Bindi, D., Zaccarelli, R., Kotha, S. R. (2021):
Local and Moment Magnitude Analysis in the Ridgecrest Region, California: Impact on Interevent Ground-Motion Variability. - Bulletin of the Seismological Society of America, 111, 1, 339-355.

https://doi.org/10.1785/0120200227

Local and moment magnitude analysis in the Ridgecrest region, California: impact on inter-event ground motion variability

Dino Bindi [1], Riccardo Zaccarelli [1], Sreeram Reddy Kotha [2]

[1] Helmholtz Centre Potsdam, GFZ German Research Centre for Geosciences, Telegrafenberg 14473, Germany

[2] Univ. Grenoble Alpes, Univ. Savoie Mont Blanc, CNRS, IRD, IFSTTAR, ISTerre, 38000 Grenoble, France.

e-mails: D. Bindi: bindi@gfz-potsdam.de; R. Zaccarelli: rizac@gfz-potsdam.de; S-R. Kotha: sreeram-reddy.kotha@univ-grenoble-alpes.fr

corresponding author: Dino Bindi

Helmholtz Centre Potsdam, GFZ German Research Centre for Geosciences, Telegrafenberg 14473, Potsdam, Germany

September 22, 2020

Abstract

We investigate the dependence of event-specific ground motion residuals in the Ridgecrest region, California. We focus on the impact of using either local (Ml) or moment (Mw) magnitude for describing the source scaling of a regional ground motion model. In order to analyse homogeneous Mw, we compute the source spectra of about 2000 earthquakes in the magnitude range 2.5-7.1 by performing a non-parametric spectral decomposition. Seismic moments and corner frequencies are derived from best fit ω^{-2} source models, and stress drop computed assuming standard circular rupture model. The Brune stress drop varies between 0.62 and 24.63 MPa (with median equal to 3.0 MPa), and values for $Mw > 5$ are mostly distributed above the 90th percentile. The median scaled energy for $Mw < 5$ is -4.57 and the low values obtained for the Mw 6.4 and 7.1 mainshocks (-5 and -5.2, respectively) agree with previous studies. We calibrate an ad-hoc non-parametric Ml scale for the Ridgecrest region. The main differences with the standard Ml scale for California are observed at distances between 30 and 100 km, where differences up to 0.4 magnitude units are obtained. Finally, we calibrate ground motion models for the Fourier amplitude spectra considering the Ml and Mw scales derived in this study and the magnitudes extracted from ComCat. The analysis of the residuals shows that Ml better describes the inter-event variability above 2 Hz. At intermediate frequencies (between about 3 and 8 Hz), the inter-event residuals for the model based on Mw show a correlation with stress drop: this correlation disappears when Ml is used. The choice of the magnitude scale has an impact also on the statistical uncertainty of the median model: for any fixed magnitude value, the epistemic uncertainty is larger for Ml below 1.5 Hz and larger for Mw above 1.5 Hz.

INTRODUCTION

The decomposition of the ground motion residuals into source, path and site specific terms is of interest for a wide spectrum of applications (Al Atik and Youngs, 2014; Baltay et al., 2017; Parker et al., 2020), such as the develpment of partially- or non-ergodic ground motion models for probabilistic hazard assessment, e.g. (Anderson and Brune, 1999; Atkinson, 2006; Rodriguez-Marek et al., 2013; Villani and Abrahamson, 2015; Kuehn and Scherbaum, 2016; Sahakian et al., 2019; Kotha et al., 2020); on-site early warning applications (Spallarossa et al., 2019; Iaccarino et al., 2020); characterization of source process such as monitoring the preparation phase of earthquake nucleation (Piña-Valdès et al., 2018; Picozzi et al., 2019) and fault healing (Bindi et al., 2018). Among the different components, the distribution of event-specific deviations from the median predictions (the so-called inter-event or between-event residuals) are connected to source processes which are only partially captured, or not described at all, by the explanatory variables used to develop the ground motion model. Since the magnitude is the most important variable controlling the source scaling, previous studies evaluated the impact of the magnitude uncertainties on the inter-event variability (Moss, 2011; Kuehn and Abrahamson, 2017; Holmgren and Atkinson, 2018) or the dependency of the inter-event residuals on stress drop for those models implementing the moment magnitude as explanatory variable, e.g. (Bindi et al., 2007; Baltay et al., 2017; Oth et al., 2017; Trugman and Shearer, 2017; Bindi et al., 2019a; Parker et al., 2020).

The aim of the present study is to investigate the ground motion variability from the source point of view, focusing over the Ridgecrest region in California. To accomplish this task, we apply a spectral decomposition approach for estimating the source parameters of selected earthquakes; for the study area, we calibrate an ad-hoc local magnitude scale which accounts for region-specific propagation effects; we develop different ground motion models considering different magnitude types, namely the local and the moment magnitudes, and the magnitude retrieved from the ANSS Comprehensive Earthquake Catalog. All these analyses are combined to investigate the ground motion variability from the event point of view, as presented in the following sections after the description of the used data set.

DATA SET

The data set used in this study was created by using *stream2segment* (Zaccarelli et al., 2019), a Python package designed for download, inspect and process seismic waveforms retrieved through International Federation of Digital Seismograph Networks-FDSN compliant webservices (see Data and Resources). The package *stream2segment* uses a seismic catalog to download data segments extracted from continuous streams stored in repositories and to populate a local relational database. The event catalog considered in this study to guide the extraction is the ANSS Comprehensive Earthquake Catalog (ComCat) created via the event webservice of the USGS-United States Geological Survey(see Data and Resources). The region of interest for the hypocenters extends between 34.5 and 36.5 in latitude, -118 and -116.5 in longitude, and depths shallower than 40 km. We consider events with magnitude above 2.5 occurred between 1999 and March 2020. Segments are extracted from both broad band and strong motion stations disseminated by IRIS (Incorporated Research Institutions for Seismology) and SCEDC (Southern California Earthquake Data Center). We downloaded data from stations located up to 2 degrees from the epicenters, extracting windows 2 minutes long after the expected theoretical P-wave arrival time and 1 minute before.

For each segments, we applied an automatic processing by removing the instrumental response, and applying Butterworth band-pass filter with lower corner fixed to 0.3, 0.1 and 0.05 Hz for magnitudes smaller than 3, between 3 and 6 and larger than 6, respectively; the upper corner was set to the minimum between 40 Hz and the 90% of the Nyquist frequency. We computed the signal to noise ratio SNR (root mean square ratio between the signal and noise spectra) over 14 frequency intervals with boundaries [f_{min},0.15,0.25,0.4,0.65,1.0, 1.6,2.5,3.2,4.0,6.3,10,16,25,f_{max}] Hz, used to select the spectral amplitudes suitable for performing the spectral decomposition. In particular, spectra with SNR computed over the whole bandwidth from f_{min} to f_{max} smaller than 3 were discarded. For the spectral analysis described in the following sections, spectral amplitudes at a given frequency are used if the SNR computed over the relevant frequency interval is karger than given threshols. In this study, we set the SNR thresholds to 3 for frequency interval below 1 Hz and above 20 Hz, and to 6 in between. The signal windows were selected considering the interval between the 2.5 and 97.5 percentiles of the cumulative distribution of the squared velocity integrals, computed starting 1 s before the theoretical P-wave arrival time. The minimum window duration was fixed to 8 s and a 5% cosine-taper was applied at both ends. For each trace, we computed the Fourier Amplitude Spectra (FAS), the peak ground acceleration (PGA) and velocity (PGV) and the maximum of a synthetic Wood-Anderson displacement record (maxWA), the latter used for computing the local magnitude. PGA and PGV are used to remove traces with anomalous values by computing the residuals with the prediction from a ground motion prediction equation (GMPE). Since the residual analysis are performed only to remove outliers, the selection of the GMPE is not critical and we used (Bindi et al., 2014). We computed the standardized average residual per station and per event, after removing the average bias from the overall residual distribution, evaluated for $vs30 = 760\ m/s$. Since the aim of the selection is not to create the most complete data set but to build a data set large enough to perform robust analysis, stations and events with respectively inter-station or inter-event standardized residuals larger than 2 in absolute value were not further considered. Overall, we selected about 190000 horizontal records from about 2000 earthquakes recorded by about 716 stations, considering co-located broad band and strong motion sensors as two different stations. Figure (1) shows the locations of considered stations and earthquakes. Most of the stations belongs to the CI network. In the following, we indicate the instruments using their $SEED$ format (Data and Resources), composed by three letters where the first is indicating the band code (always H in this study, that is high broad band, corresponding to sampling rate from 80 to 250 Hz); the second letter is the instrument code (in this study we consider high gain seismometers, letter H, or strong motion instruments, letters N and L); the third letter is the orientation code, in this study either N or E, corresponding to the horizontal orientations. The analysis described in the following sections are performed over the following data sets:

- spectral decomposition: about 112000 amplitudes (computing the vector sum of the two horizontal components, which is independent of the sensor orientation), 716 stations (counted at the level of network,station name, band and instrument codes), 2180 events, 15 contributing networks (i.e., 8E,AZ,BK,CI,NN,NP, PB,PY,SB,SN,TA,TO, US,YN,ZY including, respectively, 11,47,6,520,20,15,2, 18,6,8,3,17,1,41,1 stations, where HN, HL and HH channels are counted separately);
- local magnitude analysis: about 188000 records (the two horizontal components are considered independently); 2029 events; 508 (EW component), 515 (NS component) stations. Sensors: instrument code N=726; L=20; H=630; 14 networks;
- ground motion models: 1879 events, 649 stations, about 90000 amplitudes counted at intermediate frequencies.

Figure (2) shows the density plot of the data set used for the local magnitude calibration in terms of ComCat magnitudes versus hypocentral distance. Most of the selected data are for magnitudes between 2.5 and 5, with six earthquakes above magnitude 5 (including the 2019 Mw 6.4 and 7.1 earthquakes). The median magnitude and distance are 3.2 and 120 km, respectively, and the distributions of data with distance for different magnitude intervals are shown in Figure S1 of the Supplementary materials.

SPECTRAL DECOMPOSITION

We factorize the Fourier amplitude spectra (FAS) by applying a spectral decomposition approach known as Generalized Inversion Technique (GIT) or Global EGF approach (Andrews, 1986; Castro et al., 1990; Boatwright et al., 1991; Shearer et al., 2019). We use a non-parametric description of the FAS assumed to be the linear composition (convolution) of source $S(f)$, propagation $A(R, f)$ and site $Z(f)$ terms:

$$LogFAS_{ij}(R_{ij}, f) = LogS_i(f) + LogA(R_{ij}, f) + LogZ_j(f) \tag{1}$$

where the indexes i and j run over all available events and stations, respectively, and R_{ij} is the hypocentral distance. In the reminder of this work, we indicate with Log the logarithm in base 10. The attenuation is evaluated at fixed distances introduced to discretize the distance range into a given number of bins, and linearly interpolated between two consecutive nodes, that is:

$$LogFAS_{ij}(R_{ij}, f) = LogS_i(f) + a_n LogA(R_n, f) + a_{n+1} LogA(R_{n+1}, f) + LogZ_j(f) \tag{2}$$

where $R_n \leq R_{ij} < R_{n+1}$; $a_n = (R_{n+1} - R)/\Delta R$; $\Delta R = (R_{n+1} - R_n)$; $a_{n+1} = 1 - a_n$. We consider the following discrerization of the distance range: $R_n = [1, 3, 6, 10, 15, 20, .., 210, 215, 220]$ km. For each frequency f, a linear system is generated from equation (2) by considering all the possible combinations between i and j (corresponding to all selected recordings), and the system is solved in a least squares sense (Koenker and Ng, 2017). Since equations (1) and (2) are generated by adding together three terms, the system has not an unique solution due to the trade-offs among the factors. Therefore, GIT cannot produce absolute source and site terms and two a-priori constraints are needed to restore the uniqueness of the solution (which is a solution relative to the assumed constraints). In this study, we assume a reference distance $R_{ref} = 6$ km for the attenuation where we apply the constraint $LogA(R_{ref}, f) = 0$, and we assume a reference site condition expressed by:

$$\frac{1}{N_r} \sum_{k=1}^{N_r} LogZ_k = \Gamma(f) \tag{3}$$

where the average amplification for a set of N_r selected sites is constrained to coincide with the amplification function $\Gamma(f)$ (Pacor et al., 2016). The N_r stations are selected by performing a preliminary inversion where we constrain the logarithm of average amplification of all stations to 0. The stations selected for entering in equation (3) are picked up among those showing almost flat amplifications with amplitude below the average (see Figure S2 of the Electronic supplements). In addition, we require that the reference stations are installed at sites with measured $vs30$ (average shear wave velocity of the uppermost 30m) above 700 m/s, where the $vs30$ are extracted from (Rekoske et al., 2020). Regarding the reference amplification function $\Gamma(f)$, we considered the crustal amplification model for the National Earthquake Hazards Program (NEHRP) B/C boundary multiplied by an exponential term with $k_0 = 0.034\ s$ (Campbell and Boore, 2016). In the following, in solving equation (2), the spectral attenuation is smoothed by requiring the second derivative with distance to be small (Castro et al., 1990).

Once the source terms $S(f)$ are isolated from the other factors, seismic moments (M_0) and corner frequencies f_c are estimated by fitting a ω^{-2} model to the non-parametric source spectra, that is:

$$LogS(f) = LogK + LogM_0 + \frac{1}{1 + \left(\frac{f}{f_c}\right)^2} \tag{4}$$

The constant K in equation (4) absorbs all the constants relating the low-frequency plateau level to the seismic moment for the far-field source displacement, as well as the offset arising from the trade-off between source and site terms in equation (1). The constant K is determined by constraining the average seismic moments of earthquakes with moment magnitude $M_w < 5$ to the values extracted from the ComCat catalog. In this way, the moment magnitudes derived in this study are compatible, on average, with Mw from ComCat. Due to the limited band width towards low frequencies, individual seismic moments of events with $Mw > 5$ are constrained to the values extracted from ComCat (as shown in Figure S3a of the Supplementary materials).

GIT results

The non-parametric spectral attenuation curves are shown in Figure 3a and listed in Table S1 of the Electronic supplements. The rate of attenuation is generally increasing with frequency and the frequency dependence is stronger above 60 km. At distances approaching zero, the spectral attenuation curves tend to saturate. Curves at frequencies lower than about 5 Hz show a flat trend, or even bumps, for distances between 60 and 120 km, as consequence of secondary arrivals present within the analysed time windows, such as reflections from the mid-lower crust and Moho (Burger et al., 1987; Somerville and Yoshimura, 1990; Liu and Tsai, 2009; Chapman and Godbee, 2012). The expected travel times of Moho reflections (SmS) in the study area are shown in Figure S4 of the Electronic supplements. In Figure 3a, the attenuation curves above 20 Hz are limited to 150 km to preserve a good signal to noise ratio.

The relative site amplification functions are shown in Figure 3b, along with the reference amplification $\Gamma(f)$ entering in equation (3). With respect to the assumed reference, the site amplifications at different sites show a large variability, being the 5th and 95th percentiles separated by almost a factor 10 for frequencies below 10 Hz. Above 10 Hz, there is a strong impact of the near surface attenuation (k_0 parameter) which reduces significantly the amplification levels, although the overall variability of the site amplifications increases. A detailed discussion about the impact of site effects on ground motion variability during the Ridgecrest sequence is provided by (Parker et al., 2020).

The acceleration source spectra obtained through the non parametric GIT inversion are shown in Figure 3c. In order to determine the seismic moment M_0 and the corner frequency f_c of each event, the source spectra are fitted with an ω^{-2} model as in equation (4). The stress drop $\Delta\sigma$ is derived from the seismic moment and the source radius r (Eshelby, 1957; Keilis-Borok, 1959):

$$\Delta\sigma = \frac{7}{16}\frac{M_0}{r^3} \tag{5}$$

Assuming a circular crack model with uniform stress drop, the relationship between source radius and corner frequency f_c is given by (Brune, 1970; Madariaga, 1976):

$$r = \frac{k\beta}{f_c} \tag{6}$$

where the constant k in equation (6) depend on the assumed rupture model, and we use shear-wave velocities β derived from the 1D velocity model of (Hauksson and Unruh, 2007), fixing the P- to S-waves velocity ratio to 1.73. Ridgecrest and Indian Wells Valley regions are considered areas of relative high stress drop in southern California (Hauksson, 2015). As discussed in several studies, e.g., (Kaneko and Shearer, 2014; Trugman and Shearer, 2017; Shearer et al., 2019; Trugman, 2020), stress drop values are model dependent, with estimates conditional on the choice for the rupture model in equation (6) and on the value assumed for the high frequency falloff n (e.g., $n = 2$ in equation 4). Observed deviations from self-similarity have been related to a trade-off with n for earthquakes in California by (Trugman and Shearer, 2017; Trugman, 2020). Since our aim is not to discuss the absolute values of $\Delta\sigma$ but to use $\Delta\sigma$ for interpreting the ground motion variability, we compute $\Delta\sigma$ under standard assumptions, i.e., $n = 2$ and k= 0.38 (Kaneko and Shearer, 2014), and discussing the relative variations of the estimates. The resulting seismic moment versus corner frequencies scaling is shown in Figure 3d, where the radiated energy is computed from the squared source velocity spectra corrected for limited band effects following (Ide and Beroza, 2001). The source parameters are listed in Table S2 of the Electronic supplements.

For $Mw < 4$, the 10th, 50th, 90th percentiles of the $\Delta\sigma$ distribution are equal to 1.2, 2.9 and 7.2 MPa, respectively; for $4 \leq Mw < 5$, the median of the $\Delta\sigma$ distribution increases and the 10th, 50th and 90th percentiles become 2.6, 5. and 9.3 MPa, respectively. Above magnitude 5, the limited bandwidth towards low frequencies does not allow to estimate simultaneously M_0 and f_c. Therefore, we constrain M_0 to the values corresponding to the Mw of ComCat and we estimate the values of f_c which provide the best fit in terms of ω^{-2} model. The stress drop obtained for the four events with magnitude between 5 and 5.5 are 3.7, 5.9, 6.0, 8.9 MPa, confirming the increase of $\Delta\sigma$ for larger events. The standard deviation of the overall $Log(\Delta\sigma)$ distribution is about 0.3, smaller than typical variability observed in recent studies (0.35-0.45 Log units, e.g., (Baltay et al., 2013; Oth et al., 2017; Trugman and Shearer, 2017; Trugman, 2020)). Indeed, the $\Delta\sigma$ distribution shows both left and right tails lighter than a normal distribution (see figure S5 in the supplements), suggesting that applied data selection and processing could have censored extreme values, leading to an underestimation of the stress drop variability.

The Mw 6.4 and 7.1 mainshocks of the 2019 Ridgecrest sequence are multi-segment events that ruptured orthogonal faults, e.g. (Liu et al., 2020; Goldberg et al., 2020). The Mw 6.4 was a double earthquake where dynamic triggering allowed the rupture to jump across a step over and grown on a large fault segment (Goldberg et al., 2020; Lomax, 2020). Moreover, several studies indicated that the 6.4 event has probably statically triggered the Mw 7.1 one, e.g., (Goldberg et al., 2020; Chen et al., 2020; Qiu et al., 2020), and the rupture of the Mw 7.1 first propagated as crack-rupture and then evolved over different fault-segments as slip-pulses towards the Coso volcanic area and the Garlock fault (Chen et al., 2020). Therefore, the determination of the source parameters of the mainshocks would deserve a dedicated study. In order to extend our study of the ground motion variability also to the mainshocks, here we provide a first order assessment of $\Delta\sigma$ by considering an oversimplified model. We estimate $\Delta\sigma$ by considering an elliptical crack model with semi-axis equal to $a = L/2$ and $b = W/2$, that is:

$$\Delta\sigma = \frac{3}{4}\eta\frac{M_0}{\pi a b^2} \tag{7}$$

where η is a function of the Poisson's modulus (here assumed equal to 0.25), of the aspect ratio a/b and of the complete elliptical integrals of the first and second kind (Eshelby, 1957; Denolle and Shearer, 2016). If we use the empirical relationships of (Thingbaijam et al., 2017) for strike slip events, we obtain L=78 km, W=20.4 km for Mw 7.1 and L= 26 km, W= 13.4 km for Mw 6.4. Applying a reduction factor of 0.75 and 0.9 for L and W, respectively, to account for the fact that the actual rupture is expected to be shorter than the length and width of the entire rupture (Mai and Beroza, 2000), we obtain $\Delta\sigma$=5.2 and 7.5 MPa, for generic Mw 6.4 and 7.1 strike slip events, respectively. Several studies investigated the coseismic rupture process of the mainshocks using geodetic and seismological observations. The surface displacement caused by the Mw 7.1, as mapped by satellite images and geodetic observations, corresponds to a rupture about 46 km long (Barnhart et al., 2019; Li et al., 2020; Chen et al., 2020). For L=46km and W=15km, from equation 7 we get $\Delta\sigma$=14.7 MPa; using L=15km and W=12km for the Mw 6.4 event, we get $\Delta\sigma = 7.5MPa$. Although these values are based on oversimplified models and they could be affected by large uncertainties (at least a factor 2), in the following we use these values as first order estimates for discussing the ground motion variability.

Figure 4 summarizes the dependency of $\Delta\sigma$ on both Mw (panel a) and hypocentral depth (panel b). As shown by the 10th, 50th, and 90th quantiles of smoothing splines (Koenker et al., 1994), $\Delta\sigma$ increases with both parameters, in agreement with recent studies (Parker et al., 2020; Trugman, 2020). The Pearson correlation coefficients are significantly different from 0 at 95% confidence level and equal to 0.135 (with 95% confidence interval equal to CI=0.091-0.178) and 0.338 (CI=0.297-0.377) for the dependencies on Mw and depth, respectively. The best weighted least squares fits (for details, see Figure S6 of the Supplements to this article) are $Log(\Delta\sigma) = 0.1544Mw + 0.0058$ and $Log(\Delta\sigma) = 0.0357Z + 0.3294$, with depth Z measured in km and $\Delta\sigma$ in MPa. The slope of the magnitude dependent relationship implies an exponent ϵ for the $Mo \propto f_c^{-(3+\epsilon)}$ relationship (Kanamori and Rivera, 2004) equal to 0.1. This value of ϵ generates a departure from self-similarity weaker than the value $\epsilon = 0.21$ obtained by (Trugman, 2020) analyzing 11370 events with magnitudes mostly distributed between 2 and 2.5 (see Figure S5 for a comparison of the models). It is worth remembering that, although the spectral decomposition is expected to retrieve reliable source spectra and source parameters over the analyzed magnitude range, e.g. (Bindi et al., 2020), the choice of considering an ω^{-2} source model has an impact on ϵ. For a detailed discussion about the connection between the $n - \epsilon$ trade-off and the departure from self-similarity, see (Trugman, 2020). Regarding the dependence of $\Delta\sigma$ on depth, the slope obtained in this study is in agreement with (Trugman, 2020) (see Figure S5 of Supplements).

In Figure 4, the radiated energy is also provided. In particular, the median of logarithm of the scaled energy for $Mw < 5$ is -4.57, with [5-95]% confidence interval given by [-5.15,-4.03] (Figure 4c), where the reference value used by (Kanamori, 1977) and (Hanks and Kanamori, 1979) to define Mw for large earthquakes is $Log(5x10^{-5}) = -4.3$, see also (Choy and Boatwright, 1995). The scaled energy shows a weak dependence on seismic moment, being the slope of the best least-squares fit equal to $= 0.06 \pm 0.01$ (Figure 4d). For the two largest earthquakes, we estimated the radiated energy using teleseismic recordings and following (Di Giacomo et al., 2010). The station distribution and the distribution of the obtained station energy magnitudes are shown in Figure S7 of the Electronic supplements. The obtained energy estimates are $5.3x10^{13}$ J and $3.6x10^{14}$ J, in good agreement with the IRIS values ($5.4x10^{13}$ J and $4.8x10^{14}$ J, see Data and Resources). These values correspond to scaled energy equal to -4.98 and -5.2, values close to 15th and 5th percentiles of the distribution for $Mw < 5$ (Figure 3f). As observed by (Liu et al., 2020), low values of scaled radiated energy along with the low rupture velocity that characterized these events could suggest high fracture energy and/or longer slip-weakening distance, features that could be connected to the immaturity of the fault system.

LOCAL MAGNITUDE

In order to assign an homogeneous local magnitude to all considered earthquakes, we calibrate a local magnitude scale following a non-parametric approach (Savage and Anderson, 1995; Bindi et al., 2019b), based on a schema similar to equation (2) but applied to the Wood-Anderson maximum amplitudes:

$$LogA_{ij}(R_{ij}) = Ml_i + a_n LogA_0(R_n) + a_{n+1} LogA_0(R_{n+1}) + dMl_j^C \tag{8}$$

where A_{ij} is the maximum Wood-Anderson amplitude in mm measured for event i recorded at the hypocentral distance R_{ij}; Ml_i is the local magnitude of event i; A_0 is the zero-magnitude attenuation function determined as table of values a_n, linearly interpolated between nodes n and $n+1$, where $R_n \le R_{ij} < R_{n+1}$; dMl_j^C is the magnitude correction of station j, where C can be either north-south (NS) or east-west (EW), considering the two horizontal components as independent measurements (Uhrhammer et al., 2011). In this study, co-located strong motion (channels HN or HL) and velocimetric (channel HH) sensors are treated as two different stations sharing the same location. We synthetize the Wood-Anderson seismograms considering 2080 as gain (Uhrhammer and Collins, 1990). Regarding the reference distance where to anchor the attenuation function to the Richter one, we use $R_{ref} = 17\ km$ (Hutton and Boore, 1987) and we constrain the station corrections dMl_{Ω}^{C} for a set of stations $j \in \Omega$ to zero. We use as reference set Ω the same set of stations used for the spectral decomposition.

Magnitude results

Figure 5 compares the calibrated $LogA_0$ function (listed in Table S3 of the Electronic supplements) with both the parametric models for Southern California (Hutton and Boore, 1987) and the attenuation function proposed by (Uhrhammer et al., 2011) to integrate the models developed for southern and northern California. The 100 bootstrap curves show a very narrow spread, meaning that the median model is well constrained by data and it shows a low epistemic uncertainty. Only below 3 km the spread is visible, as expected from the reduced data availability. The attenuation is similar to (Uhrhammer et al., 2011) for CISN (California Integrate Seismological Network) in the distance range from 3 to 20 km; between 20 and 60 km, the non-parametric model shows a faster decay than CISN and Southern California models, reaching a difference up to 0.3-0.4 magnitude units around 60 km. Between 60 and 120 km, the non-parametric model shows a weaker attenuation, similar to the behavior observed for the spectral attenuation at intermediate frequencies (Figure 3), bringing $LogA_0$ close to the parametric models. Above 120 km, the attenuation rate is similar to the rate of the CISN model. The behavior of the $LogA_0$ functions suggest that between 30 and 100 km, some differences in the station magnitudes computed using our model should be expected. The attenuation model derived in this study deviates from the trend of the (Uhrhammer et al., 2011) and (Hutton and Boore, 1987) models also below 3 km; although these distances are not well sampled by data, the obtained saturation agrees with the expectations from (Luckett et al., 2018) and the results obtained for Europe by (Bindi et al., 2019b).

The magnitude station corrections are shown in Figure 6 (and listed in Table S4 of the Electronic supplements), where the results for the two horizontal components are compared with the station correction of the CISN model. For the HN and HL channels, we compared dML^{C} with the CISN correction computed for the co-located HH channel. The magnitude corrections show a good correlation (please note that the correction has opposite sign between respective models), with the tendency of the

CISN corrections to saturate for positive values (rock-like sites) with respect to this study. The crosses in Figure 6 indicate the stations in the reference set Ω. A linear regression $dM^C = (a + b \ \ dM_{CISN})$ considering the HH channels produces the best fit models $(a, b) = (0.17 \pm 0.01, -0.96 \pm 0.05)$ and $(a, b) = (0.16 \pm 0.01, -0.94 \pm 0.05)$ for the EW and NS components, respectively. The offset between the two set of magnitude corrections is connected to different choices for set of reference stations. The median CISN corrections for the reference stations in Ω are 0.15 and 0.18 for the EW and NS components, respectively, values close to the intercept of the best fit linear models.

The local magnitudes computed in this study are shown in Figure 7, along with the magnitude values extracted from ComCat. The preferred magnitudes disseminated through ComCat are mostly local (below 3.5) or moment (above 3.5) magnitudes but, between magnitude 3 and 6, a revised local magnitude (named Mlr) is also computed. Mlr was introduced by SCEDC in late 2015 to reduce the over-estimation of Ml with respect to Mw for earthquakes above magnitude 3.5 in California. The local magnitudes are in good agreement, being the values obtained in this study 0.08 m.u. larger on average than the catalog ones, whereas Mw and Mlr are on average 0.24 m.u. larger than Ml from this study. The best fit least squares model for the relationship between the local magnitudes derived in this study with respect to ComCat is shown in Figure S3b of the Electronic supplements. Figure 8 compares the station corrections dMl^C with the GIT site amplifications extracted for three frequencies, 0.5, 3 and 10 Hz. We recall that the synthesized Wood-Anderson recordings are high pass filtered displacement waveforms, since this instrument has a corner frequency at 1.25 Hz (i.e., a period of 0.8 s). As expected, the magnitude station corrections show the strongest correlation with the site amplifications at intermediate frequencies, around 3 Hz, whereas filtering effects of the instrument, high frequencies amplifications and near-surface attenuation effects reduce the correlation below 1 Hz and above 10 Hz.

GROUND MOTION MODELS

We calibrate a Ground Motion Model (GMM) for the amplitude Fourier spectra, considering the following model:

$$LogFAS = F(M) + G(n_1, n_2, n_3; Log(R), R_a, R_b) + Q(k_1; k_2; R, R_a, R_b) + \delta B_e + \delta S2S + \epsilon \qquad (9)$$

where the magnitude term is given by:

$$F(M) = e_1 + b_1(M - 3.5) + b_2(M - 3.5)^2 \tag{10}$$

and the distance-dependent attenuation terms are given by:

$$G(n_1, n_2, n_3; Log(R), R_a, R_b) =$$

$$= \begin{cases} n_1 Log(\frac{R}{6}) & \text{if } R \leq R_a \\ n_1 Log(\frac{R_a}{6}) + n_2 Log(\frac{R}{R_a}) & \text{if } R_a < R \leq R_b \\ n_1 Log(\frac{R_a}{6}) + n_2 Log(\frac{R_b}{R_a}) + n_3 Log(\frac{R}{R_b}) & \text{otherwise} \end{cases} \tag{11}$$

$$Q(k; R, R_a, R_b) =$$

$$= \begin{cases} 0 & \text{if } R < R_a \\ k_1(R - R_a)/100 & R_a \leq R < R_b \\ k_1(R_b - R_a)/100 + k_2(R - R_b)/100 & \text{otherwise} \end{cases} \tag{12}$$

In equation 9, δB_e are inter-event random effects described by a normal distribution with zero mean and standard deviation τ; $\delta S2S$ are the inter-station random effects described by a zero mean normal distribution with standard deviation ϕ_{S2S}; ϵ are the event and station corrected residuals, described by a zero mean normal distribution with standard deviation ϕ. Following the spectral decomposition analysis, the hinge distances R_a and R_b in equations (11) and (12) are fixed to 10 and 60 km, respectively. The model in equation (9) is calibrated three times, each time considering a different magnitude scale, i.e. local, moment and catalog magnitudes.

Results GMM

The coefficients of GMMs developed for the three magnitude scales are listed in Tables S5 through S13, along with their errors and the standard deviations of the residual distributions. Figure 9 shows the distance scaling of the GMM for different frequencies, along with attenuation values averaged over different frequency intervals. The main attenuation features shown by parametric distance scaling resemble those obtained with the non-parametric spectral decomposition (Figure 3) with stronger frequency dependence above 60 km and with a flattening or bumps in the attenuation curves between about 60 and 120 km for low frequencies. The GMMmedian model describes well both the attenuation and source scaling of the spectral amplitudes, as confirmed by the distribution of the residual ϵ versus magnitude and distance, exemplified in Figure 10 at 3 Hz.

The standard deviations of the different random effects are compared in Figure 11 for the three magnitude choices. The overall aleatory variability σ is dominated by site contribution ϕ_{S2S}, which shows a strong increase above 10 Hz, in agreement with the variability of the site amplifications from the spectral decomposition shown in Figure 3. The large site to site variability observed at high frequencies is a characteristics of the ground motion models when derived in the Fourier domain instead of for response spectra, as discussed by (Bindi et al., 2017), and already observed for California by (Bayeless and Abrahamson, 2019) (their Figure 12) and for Europe by (Bindi et al., 2019c) (their Figure 13). The inter-event variability τ is providing the lowest contribution and only marginally impact over the overall variability σ at low or intermediate frequencies, depending on the magnitude type. We will discuss the dependency of τ on the selected magnitude in the next sections, using the results from the different analysis performed in this study.

DISCUSSIONS

The earthquake size is captured differently by different magnitude scales (Choy and Boatwright, 1995; Bormann and Di Giacomo, 2011): while Mw is measuring the earthquake size from the static point of view (seismic moment), Ml is influenced by dynamic characteristics of the rupture process such as rupture velocity and stress drop (Deichmann, 2017, 2018). Therefore, the aleatory variability of the inter-event residuals δB_e is expected to be influenced by the choice on the magnitude scale considered as explanatory variable, and the differences are expected to be frequency dependent. These expectations are confirmed by the values of the standard deviation τ shown in Figure 11: when Mw is used, τ is the lowest at low frequencies (below 1 Hz) whereas τ for Ml becomes the lowest at intermediate frequencies, around 3 Hz. At high frequencies, τ for Ml is still lower than for Mw whereas τ for the ComCat magnitudes (which is a mixture of local and moment magnitudes) is never the lowest.

The differences in τ are further inspected in Figure 12 by looking at the inter-event residual distribution at 0.72 Hz and 3 Hz. At 3 Hz, the distribution for Ml is much narrower than for Mw, indicating that the median model for Ml better captures the source related variability of spectral amplitudes at intermediate frequencies, where most of the corner frequencies of the analysed data set are distributed. Moving towards lower frequencies, the δBe distribution for Mw becomes the narrowest, as expected over a frequency range controlled by the seismic moment.

The dependence of δB_e on the implemented magnitude type has also an impact on the statistical uncertainty (epistemic) of the median model, often referred to as σ_μ (Al Atik and Youngs, 2014). Figure 13 shows σ_μ for different scenarios corresponding to magnitudes (Ml and Mw) varying from 3 to 7 and fixing the hypocentral distance at 30 km. Several features are shown by σ_μ: it increases with magnitude, in particular above magnitude 5; it is larger for Ml at low frequencies and for Mw at high frequencies; for $Mw = 7$, σ_μ has a broad minimum between about 0.6 and 2 Hz and, decreasing the magnitude, this range broadens; for $Ml = 7$, σ_μ shows a narrow minimum around 3 Hz and, decreasing the magnitude, the minimum broadens; for a magnitude 7, σ_μ is smaller for Ml at 3 Hz than for Mw at 0.8 Hz. Finally, considering the same magnitude value, the σ_μ curves for Mw and Ml crosses close to 1.5 Hz, i.e., for any fixed magnitude value, the epistemic uncertainty is larger for Ml below 1.5 Hz and larger for Mw above 1.5 Hz. Therefore, the epistemic uncertainty depends on the magnitude type and which is the preferred type (minimization of σ_μ) depends on the frequency range of interest.

Since the $\Delta\sigma$ variations leave an imprint in Ml, the reduction of τ for Ml around 3 Hz is expected if the inter-event residuals at intermediate/high frequencies show some degree of correlation with $\Delta\sigma$. The spectral decomposition analysis showed that the variability of $\Delta\sigma$ is pretty limited for the analysed data set, about a factor 10. To enhance the detection of a correlation between δBe and $\Delta\sigma$, Figure 14 compares trend analysis between δBe and $\Delta\sigma$ considering the GMMs for Ml and Mw and 6 different frequencies between 0.5 Hz and 10 Hz. The trend curves are the results of fitting a generalized additive model to data, using cubic regression splines (see Data and Resources). At low frequencies (0.5 Hz), there is not correlation considering Mw and a negative correlation for Ml. We can explain this negative correlation with the fact that a large stress drop implies a Ml larger than Mw and since this Ml is used over the whole frequency range, it causes over predictions at low frequencies which are controlled by Mw. Increasing the frequency, the correlation for Ml disappears and the correlation for the Mw model increases, in particular between 3 and 6 Hz. At high frequencies (10 Hz in Figure 14), the

δBe variability is influenced not only by $\Delta\sigma$ and the correlation weakens. We can conclude that also for the analyzed data set, there is a dependency of δB_e on $\Delta\sigma$ at intermediate frequencies which is captured by considering Ml as explanatory variable; this choice anyway implies a degradation of the performances at low frequencies.

The scaling between Ml and Mw is shown in Figure 15a. We fit a linear model with one break-point by applying a segmented regression (Muggeo, 2003). The obtained optimal break point (BP) is located at $Mw_{BP} = 4.2 \pm 0.05$ and the slopes are 1.25, with 5-95 confidence interval given by CI=[1.23-1.26], and 0.88, with CI=[0.82-0.94], below and above Mw_{BP}, respectively. The intercept of the best fit model is -0.69 and the very high coefficient of determination $R^2 = 0.97$ suggests that model well capture the data variability. Theoretical expectations (Deichmann, 2017) are a one-to-one scaling for large events (over the range for which Ml is not saturating) and $Ml \propto 1.5Mw$ for events below a certain threshold magnitude. The values obtained for the study area are very similar to those obtained the central Italy by (Malagnini and Munafò, 2018), who found a break-point located at about $Ml = 4.3$ and slopes 2/3 for the branch below the break-point and 1.28 for the upper branch. For the Ridgecrest region, (Trugman, 2020) found a slightly steeper relationship for low magnitudes, i.e., $Mw \propto 0.74Ml$, in very good agreement with the model derived by (Ross et al., 2016) for the region around the San Jacinto fault zone (southern California). Indeed, if we extrapolate the model derived in this study towards lower magnitudes, we obtain both a slightly weaker scaling and a positive offset with respect to the model derived by (Trugman, 2020) (see Figure S3c of the Electronic supplements). These differences could be ascribed to both the extrapolation towards magnitude much smaller than those used in the calibration of this study and to biases that could affect the magnitude scales used in the different studies (gray filled ribbon in Figure S3c).

For a given event moment magnitude, the spread over the corresponding Ml values scales with $\Delta\sigma$. Figure 15b shows the dependence of $\Delta M = Ml - Mw$ on stress drop. Grouping Mw into three intervals (i.e., $3 \leq Mw$; $3 < Mw \leq 3.5$; $3.5 < Mw \leq 6$), the best fit lines are $\Delta M = -0.073 + 0.149Log(\Delta\sigma)$, $\Delta M = 0.007 + 0.211Log(\Delta\sigma)$, and $\Delta M = 0.075 + 0.281Log(\Delta\sigma)$, respectively, with $\Delta\sigma$ in MPa. These relationships confirm that the differences between Mw and Ml are a first order indicator for stress drop variability.

CONCLUSIONS

In this study, we evaluated the impact of the magnitude selection on the event-specific ground motion variability associated to a ground motion model calibrated for the Ridgecrest region in California. In order to develop the model and to discuss the inter-event residuals, we performed a spectral decomposition to obtain the source parameters, in particular an estimate of the seismic moment for all events and their Brune stress drop, and we calibrated an ad-hoc local magnitude scale. The main conclusions of the spectral decomposition analysis are:

- attenuation: the spectral attenuation curves confirmed the important role played by secondary arrivals, such as reflections from main crustal discontinuities, in modulating the spectral amplitude decay at low-intermediate frequencies. In particular, the attenuation curves show a flattening and bumps over hypocentral distances between 60 and 120 km and for frequencies below 6 Hz.

- site amplification: below 10 Hz, the site amplifications show a large variability, of the order of a factor 10; above 10 Hz, the near surface attenuation described through the kappa parameter, strongly reduce the amplifications but the overall variability increases.

- source: the spectral decomposition provided the non-parametric source spectra for about 2000 earthquakes; seismic moments and corner frequencies were obtained fitting an ω^{-2} source model and the stress drop computed considering the Brune circular rupture model. The 5th and 95th percentiles of the $\Delta\sigma$ distribution are 1 and 9.2 MPa, respectively, with median equal to 3. MPa; stress drop values increase with both depth and magnitude, showing a weak departure from self-similarity. The median scaled energy (radiated energy to seismic moment ratio) of earthquakes with $Mw < 5$ is -4.57; the Mw 6.4 and 7.1 mainshocks are characterized by very low scaled energy (-5 and -5.2, respectively), in agreement with previous studies.

The calibration of a non-parametric local magnitude scale for the study area showed that the magnitude attenuation function has a decay similar to the (Uhrhammer et al., 2011) model for distances between 3 and 25 km, and for distances above 120 km, but the models deviate between 25 and 120 km. Secondary arrivals observed for the spectral analysis have also an impact on the magnitude attenuation function and differences up to 0.4 magnitude units with respect to previous calibrated parametric models are observed for distances between 30 and 100 km; for distances below 3 km, the model calibrated in this study shows saturation of the attenuation. Regarding the station corrections, they are in good agreement with those calibrated by (Uhrhammer et al., 2011), and they show also a good correlation with the amplifications obtained through the spectral decomposition at intermediate frequencies, around 3 Hz. When Ml is compared with Mw, the local versus moment magnitude scaling is well described by a piece-wise linear model with break-point at $Ml = 4.2$ and slopes 1.25 and 0.88 for the lower and upper branch, respectively. Moreover, the difference between the local and moment magnitudes is a first order indicator for the $\Delta\sigma$ variability.

Finally, merging all results together, we conclude that the selection of the magnitude scale has a strong impact on the inter-event residuals and, in particular, on the frequency dependence of their standard deviation τ. Mw better describes the inter-event variability below 2 Hz whereas Ml better captures the variability at higher frequencies, with a minimum τ around 3 Hz. At intermediate frequencies (between 3 and 8 Hz, about), the inter-event residuals for the GMM based on Mw show a correlation with stress drop; this correlation disappears when Ml is used. The choice of the magnitude type used as explanatory variable has an impact also on the statistical uncertainty σ_μ of the median model: for any fixed magnitude value, the epistemic uncertainty is larger for Ml below 1.5 Hz and larger for Mw above 1.5 Hz. In conclusion, future effort should be devoted to the development of ground motion models where the source component is not only constructed over the moment magnitude (earthquake size) but includes also predictors informative for dynamic features of the rupture process (earthquake strength).

Data and Resources

Seismological data used in this study have been downloaded from IRIS, Incorporated Research Institutions for Seismology ($https://www.iris.edu$) and Southern California Earthquake Data Center, SCEDC ($https://scedc.caltech.edu/index.html$). The ANSS Comprehensive Earthquake Catalog, ComCat ($https://earthquake.usgs.gov/data/comcat/$) has been download from United States Geological Survey, USGS webservice ($http://earthquake.usgs.gov/fdsnws/event/1/query$).

The software stream2segment is available at $https://github.com/rizac/stream2segment$; the International Federation of Digital Seismograph Networks-FDSN specifications are available at $http://www.fdsn.org/$ and, in particular, the Standard for the Exchange of Earthquake Data (SEED) manual is available at $http://www.fdsn.org/pdf/SEEDManual$.

The IRIS energy estimates for the Mw 6.4 and 7.1 earthquakes, determined following (Convers and

Newman, 2011), are available at https://doi.org/10.17611/DP/EQE.1. Maps have been prepared with Generic mapping tools-GMT (Wessel et al., 2013). In Figure 1, focal mechanisms have been taken from Global Centroid Moment Tensor project-CMT (https:// www.globalcmt.org), Quaternary faults from USGS (https://www.usgs.gov/natural-hazards/), topography from Shuttle Radar Topography Mission project-SRTM (Jarvis et al., 2008). Travel time and efficiency computations for Figure S3 have been performed with Pyrocko (Heimann et al., 2017), available at *https://pyrocko.org/*. The derivation of the models was performed using R software (R Core Team, 2018) and, in particular, ggplot2 (Wickham, 2016), sparseM (Koenker and Ng, 2017), Matrix (Bates and Maechler, 2017), dplyr (Wickham et al., 2018), minpack.lm (Elzhov et al., 2016). All webpages last visited on April 2020.

Acknowledgments

The authors thank F. Cotton and A. Strollo for their suggestions that have resulted in several improvements to an early version of this work. Associate Editor A. Rodriguez-Marek and two anonymous Reviewers are also acknowledged for their constructive comments. This work has been developed in the framework of the URBASIS project (H2020/Marie Skodowska-Curie Actions, agreement number 813137).

References

Al Atik, L. and R. R. Youngs (2014). Epistemic uncertainty for NGA-West2 models, *Earthquake Spectra* **30**(3):1301-1318

Anderson, J.G., Brune, J.N. (1999). Probabilistic seismic hazard analysis without the ergodic assumption, *Seism Res Letters* **70**, 19-28.

Andrews, D.J. (1986). Objective determination of source parameters and similarity of earthquakes of different size, in Earthquake Source Mechanics, 259-267, eds Das, S., Boatwright, J. and Scholz, C.H., American Geophysical Union, Washington.

Atkinson, G.M. (2006). Single-station sigma *Bull. Seism. Soc. Am.* **96**, 446-455

Baltay, A. S., T. C. Hanks, and G. C. Beroza (2013). Stable stress-drop measurements and their variability: Implications for ground- motion prediction, *Bull. Seism. Soc. Am.* **103**, no. 1, 211-222, doi: 10.1785/0120120161.

Baltay, A.S., T. C., Hanks, and N. A. Abrahamson (2017). Uncertainty, variability, and earthquake physics in ground-motion prediction equations, *Bull. Seism. Soc. Am.* **107**, 1754-1772

Barnhart, W. D., Hayes, G. P., and Gold,R. D. (2019). The July 2019 Ridgecrest, California, earthquake sequence: Kinematics of slip and stressing in crossfault ruptures, *Geophys. Res. Lett.* **46**, 11,859-11,867. doi: 10.1029/2019GL084741

Bates, D. and Martin Maechler (2017). Matrix: Sparse and Dense Matrix Classes and Methods. R package version 1.2-12. $https://CRAN.R-project.org/package=Matrix$

Bayless, J., and N. A. Abrahamson (2019). Summary of the BA18 ground-motion model for Fourier amplitude spectra for crustal earthquakes in California, *Bull. Seism. Soc. Am.* **109**, 2088-2105, doi: 10.1785/0120190077

Bindi, D., Parolai, S., Grosser, H., Milkereit, C., and E. Durukal (2007). Empirical ground-motion prediction equations for northwestern Turkey using the aftershocks of the 1999 Kocaeli earthquake, *Geophys. Res. Lett.* **34**, L08305. doi: 10.1029/2007GL029222

Bindi, D., M., Massa, L., Luzi, G. Ameri, F. Pacor, R. Puglia, and P. Augliera (2014). Pan-European ground-motion prediction equations for the average horizontal component of PGA, PGV, and 5%-damped PSA at spectral periods up to 3.0 s using the RESORCE dataset, *Bull Earthq Eng* **12**, 391-430

Bindi, D., D. Spallarossa, and F. Pacor (2017). Between-event and between-station variability observed in the Fourier and response spectra domains: comparison with seismological models, *Geophys. J. Int.* **210**, 1092-1104. doi: 10.1093/gji/ggx217

Bindi, D., Cotton F., Spallarossa D., Picozzi M., and E. Rivalta (2018). Temporal variability of ground shaking and stress drop in Central Italy: a hint for fault healing? *Bull. Seism. Soc. Am.* **108**, 1853-1863. doi: 10.1785/0120180078

Bindi D, M. Picozzi, D. Spallarossa, F. Cotton, S.R. Kotha (2019a). Impact of magnitude selection on aleatory variability associated with ground motion prediction equations: part II-analysis of the between-event distribution in central Italy, *Bull. Seism. Soc. Am.* **109**, 251-262

Bindi, D., R. Zaccarelli, A. Strollo and D. Di Giacomo (2019b). Harmonized local magnitude attenuation function for Europe using the European Integrated Data Archive (EIDA), *Geophys. J. Int.* **218**, 519-533, doi: 10.1093/gji/ggz178

Bindi, D., S.-R., Kotha, G., Weatherill, G., Lanzano, L., Luzi, and F. Cotton (2019c). The panEuropean engineering strong motion (ESM) flatfile: consistency check via residual analysis, *Bull Earthq Eng* **17**, 583-602, doi: 10.1007/s10518-018-0466-x

Bindi, D., D. Spallarossa, M. Picozzi and P. Morasca (2020). Reliability of source parameters for small events in central Italy: insights from spectral decomposition analysis applied to both synthetic and real data, *Bull. Seism. Soc. Am.*, **XX**, 1-19, doi: 10.1785/0120200126

Boatwright, J., J. B. Fletcher, and T. E. Fumal (1991). A general inversion scheme for source, site and propagation characteristics using multiply recorded sets of moderate-sized earthquakes, *Bull. Seism. Soc. Am.* **81**, 1754-1782

Bormann, P. and D. Di Giacomo (2011). The moment magnitude Mw and the energy magnitude Me:common roots and differences, *Journal of Seismology* **15**, 411-427. doi: 10.1007/s10950-010-9219-2

Brune, J. N. (1970). Tectonic stress and the spectra of shear waves from earthquakes, *J. Geophys. Res.* **75**, 49975009.

Burger, R. W., P. G. Somerville, J. S. Barker, R. B. Herrmann, and D. V. Helmberger (1987). The effect of crustal structure on strong ground motion attenuation relations in eastern North America, *Bull. Seism. Soc. Am.* 77, 420-439.

Campbell, K. W. and D. M. Boore (2016). Evaluation of Six NEHRP B/C Crustal Amplification Models Proposed for Use in Western North America, *Bull. Seism. Soc. Am.* **106**, 673-686, doi: 10.1785/0120150242

Castro, R. R., J. G. Anderson, and S. K. Singh (1990). Site response, attenuation and source spectra of S waves along the Guerrero, Mexico, subduction zone, *Bull. Seism. Soc. Am.* **80**, 1481-1503.

Chapman, M. C., and R. W. Godbee (2012). Modeling geometrical spreading and the relative amplitudes of vertical and horizontal high-frequency ground motions in Eastern North America, *Bull. Seism. Soc. Am.* **102**, doi: 10.1785/0120110081

Chen, K., J-P. Avouac, S. Aati, C. Milliner, F. Zheng and C. Shi (2020). Cascading and pulse-like ruptures during the 2019 Ridgecrest earthquakes in the Eastern California Shear Zone, *Nature Communications* **11**, doi:10.1038/s41467-019-13750-w

Choy, G. L., and J. Boatwright(1995). Global patterns of radiated seismic energy and apparent stress. *J. Geophys. Res.* **100**(18), 205-226, doi: 10.1029/95JB01969

Convers, J. A., and A. V. Newman (2011), Global Evaluation of Large Earthquake Energy from 1997 Through mid-2010, *J. Geophys. Res.* **116** B08304, doi:10.1029/2010JB007928

Deichmann, N. (2017). Theoretical basis for the observed break in M_L/Mw scaling between small and large earthquakes, *Bull. Seism. Soc. Am.* **107**, doi: 10.1785/0120160318.

Deichmann, N. (2018). Why does M_L scale 1:1 with 0.5log E_s?, *Seim. Res. Letters* **89**, 2249-2255

Denolle, M.A., and P. M. Shearer (2016). New perspectives on self-similarity for shallow thrust earthquakes, *J Geophys Res Solid Earth* **121**, 6533-6565

Di Giacomo, D., S. Parolai,P. Bormann,H. Grosser,J. Saul, R. Wang and J. Zschau (2010). Suitability of rapid energy magnitude determinations for emergency response purposes, *Geophys. J. Int.* **180**, 361-374, doi: 10.1111/j.1365-246X.2009.04416.x

Efron, B. (1979). Bootstrap methods, another look at the jackknife, *Ann.Stat.* **7**, 1-26.

Elzhov,T. V., K. M. Mullen, A.-N. Spiess and Ben Bolker (2016). minpack.lm: R Interface to the Levenberg-Marquardt Nonlinear Least-Squares Algorithm Found in MINPACK, Plus Support for Bounds. R package version 1.2-1. https://CRAN.R-project.org/package=minpack.lm

Eshelby, J. D. (1957). The determination of the elastic field of an ellipsoidal inclusion, and related problems, *Proc. Math. Phys. Sci.* **241**,376-396.

Goldberg, D. E., Melgar, D., Sahakian, V. J., Thomas, A. M., Xu, X., Crowell, B. W., and J. Geng (2020). Complex rupture of an immature fault zone: A simultaneous kinematic model of the 2019 Ridgecrest, CA earthquakes, *Geophys. Res. Lett.* **47**, e2019GL086382.doi:10.1029/2019GL086382

Hanks, T. C.and H. Kanamori (1979). A moment magnitude scale, *J. Geophys. Res.* **84**, 2348-2350,doi: 10.1029/JB084iB05p02348

Hauksson, E., and J. Unruh (2007). Regional tectonics of the Coso geothermal area along the intracontinental plate boundary in central eastern California: Three-dimensional Vp and Vp/Vs models,spatial-temporal seismicity patterns, and seismogenic deformation, *J. Geophys. Res.* **112**, no. B6, doi: 10.1029/2006JB004721.

Hauksson E. (2015). Average Stress Drops of Southern California Earthquakes in the Context of Crustal Geophysics: Implications for Fault Zone Healing, *Pure Appl. Geophys.* **172**, 1359-1370

Heimann, S., M. Kriegerowski, M. Isken, S. Cesca, S. Daout, F. Grigoli, C. Juretzek, T. Megies, N. Nooshiri, A. Steinberg, H. Sudhaus, H. Vasyura-Bathke, T. Willey and T. Dahm (2017): Pyrocko - An open-source seismology toolbox and library. V. 0.3. GFZ Data Services. http://doi.org/10.5880/GFZ.2.1.2017.001

Holmgren, J. M., and G. M. Atkinson (2018). Effect of uncertainty in source parameters on ground-motion variability for potentially induced earthquakes in the central United States, *Seismol. Res. Lett* **89** 2A, 702-711. doi: 10.1785/0220170208

Hutton, L. K., and D. M. Boore (1987). The M_L scale in Southern California,*Bull. Seism. Soc. Am.* **77**, 2074-2094.

Iaccarino, A. G., M. Picozzi, D. Bindi, and D. Spallarossa (2020). Onsite Earthquake Early Warning: Predictive Models for Acceleration Response Spectra Considering Site Effects, *Bull. Seism. Soc. Am.* **110**, 1289-1304., doi: 10.1785/0120190272

Ide S., and G. C. Beroza (2001). Does apparent stress vary with earthquake size?, *Geophys. Res. Lett.* **28**, 3349-3352.

Jarvis A., H.I. Reuter, A. Nelson, E. Guevara, (2008). Hole-filled seamless SRTM data V4, International Centre for Tropical Agriculture (CIAT), available from http://srtm.csi.cgiar.org.

Kanamori, H (1977). The energy release in great earthquakes, *J. Geophys. Res.* **82**, 2981-2876, doi: 10.1029/JB082i020p02981

Kanamori, H., and L. Rivera (2004). Static and dynamic scaling relations for earthquakes and their implications for rupture speed and stress drop, *Bull. Seism. Soc. Am.* **94**, no. 1, 314-319, doi:10.1785/0120030159.

Kaneko, Y. and P. M. Shearer (2014). Seismic source spectra and estimated stress drop derived from cohesive-zone models of circular subshear rupture *Geophys. J. Int.* **197** 1002-1015, doi:10.1093/gji/ggu030

Keilis-Borok, V. (1959). On the estimation of the displacement in an earthquake source and of source dimension, *Ann. Geophys.* **12**, 205-214.

Koenker, R., P. Ng and S. Portnoy (1994). Quantile smoothing splines, *Biometrika* **81**, 673-680.

Koenker, R. and P. Ng (2017). SparseM: Sparse Linear Algebra, R package version 1.77, $https : //CRAN.R-project.org/package = SparseM$

Kotha, S. R., G. Weatherill, D. Bindi and F. Cotton (2020). A regionallyadaptable groundmotion model for shallow crustal earthquakes in Europe, *Bull Earth Eng* **XX**, doi: 10.1007/s10518-020-00869-1

Kuehn N.M., and F. Scherbaum (2016). A partially non-ergodic ground-motion prediction equation for Europe and the Middle East. *Bull Earthq Eng* **14**, 2629-2642

Kuehn,N. M.,and N. A. Abrahamson (2017). The Effect of Uncertainty in Predictor Variables on the Estimation of GroundMotion Prediction Equations. *Bull. Seism. Soc. Am.* **108**,358-70. doi:10.1785/0120170166

Li S., G. Chen, T. Tao, P. He, K. Ding, R. Zou, J. Li and Q. Wang (2020). The 2019 Mw 6.4 and Mw 7.1 Ridgecrest earthquake sequence in Eastern California: rupture on a conjugate fault structure revealed by GPS and InSAR measurements, *Geophys. J. Int.* **221**, 1651-1666. doi: 10.1093/gji/ggaa099

Liu, K-S., and Y-B Tsai (2009). Large effects of Moho reflections (SmS) on peak ground motion in Northwestern Taiwan, *Bull. Seism. Soc. Am.* **99**, 255-267, doi: 10.1785/0120080258

Liu, C., Lay, T., Brodsky, E. E., Dascher-Cousineau, K., and X. Xiong (2019). Coseismic rupture process of the large 2019 Ridgecrest earthquakes from joint inversion of geodetic and seismological observations,*Geophys. Res. Lett.* **46**, 11820-11829. doi: 10.1029/2019GL084949

Lomax, A. (2020). Absolute Location of 2019 Ridgecrest Seismicity Reveals a Shallow Mw 7.1 Hypocenter, Migrating and Pulsing Mw 7.1 Foreshocks, and Duplex Mw 6.4 Ruptures, *Bull. Seism. Soc. Am.* **XX**, 1-14, doi: 10.1785/0120200006

Luckett, R., Ottemöller, L., Butcher, A., and B. Baptie (2018). Extending local magnitude ML to short distances, *Geophys. J. Int.*, **216**, 1145-1156.

Luzi, L., D. Bindi., R. Puglia, F. Pacor, and A. Oth (2014). Single-station sigma for Italian strong-motion stations, *Bull. Seism. Soc. Am.* **104**, 467-483, doi: 10.1785/0120130089

Madariaga, R., (1976). Dynamics of an expanding circular fault, *Bull. Seism. Soc. Am.* **66**, 639-666.

Mai, P.M., and G. C. Beroza (2000). Source scaling properties from finite-fault-rupture models. *Bull. Seism. Soc. Am.* **90**, 604615

Malagnini, L. and I. Munafò (2018). On the Relationship between M_L and M_w in a Broad Range: An Example from the Apennines, Italy, *Bull. Seism. Soc. Am.* **108**, 1018-1024, doi: 10.1785/0120170303

Moss R. E. S. (2011). Reduced sigma of groundmotion prediction equations through uncertainty propagation, *Bull. Seism. Soc. Am.* **101**, 250-257, doi: 10.1785/0120090325.

Muggeo, V.M.R. (2003). Estimating regression models with unknown break-points, *Stat. Med.* **22**, 3055-3071.

Oth, A., H. Miyake, and D. Bindi (2017). On the relation of earthquake stress drop and ground motion variability, *J. Geophys. Res.* **122**, 5474-5492, doi: 10.1002/2017JB014026.

Pacor, F., D. Spallarossa, A. Oth, L. Luzi, R. Puglia, L. Cantore, A. Mercuri, M. D'Amico, and D. Bindi (2016). Spectral models for ground motion prediction in the L'Aquila region (central Italy): Evidence for stress-drop dependence on magnitude and depth, *Geophys. J. Int.* **204**, 697-718.

Parker, G. A., A. S. Baltay, J. Rekoske, and E. M. Thompson (2020). Repeatable Source, Path, and Site Effects from the 2019 M 7.1 Ridgecrest Earthquake Sequence, *Bull. Seism. Soc. Am.* **XX**, 1-19, doi: 10.1785/0120200008

Picozzi, M., D. Bindi, A. Zollo, G. Festa and D. Spallarossa (2019). Detecting long-lasting transients of earthquake activity on a fault system by monitoring apparent stress, ground motion and clustering, *Sci Rep***9**,16268. doi: 10.1038/s41598-019-52756-8

Piña-Valdès, J., Socquet, A., and F. Cotton (2018). Insights on the Japanese subduction megathrust properties from depth and lateral variability of observed ground motions. *J. Geophys. Res.*, **123**, 8937-8956. doi: 10.1029/2018JB015743

Qiu, Q., S. Barbot, T. Wang, and S. Wei (2020). Slip Complementarity and Triggering between the Foreshock, Mainshock, and Afterslip of the 2019 Ridgecrest Rupture Sequence, *Bull. Seism. Soc. Am.* **XX**, 1-15, doi: 10.1785/0120200037

R Development Core Team (2018). R: A language and environment for statistical computing, R Foundation for Statistical Computing, Vienna, Austria, available at https://www.r-project.org/ (last accessed June 2018).

Rekoske, J. M., E. M. Thompson, M. P. Moschetti, M. G. Hearne, B. T. Aagaard, and G. A. Parker (2020). The 2019 Ridgecrest, California, Earthquake Sequence Ground Motions: Processed Records and Derived Intensity Metrics, *Seismol. Res. Lett.* **XX**, 1-14, doi: 10.1785/0220190292.

Richter, C. (1935). An instrumental earthquake magnitude scale, *Bull. Seism. Soc. Am.* **25**, 1-32.

Rodriguez-Marek A., Cotton F. Abrahamson N. A. Akkar S. Al Atik L. Edwards B. Montalva G. A., and H. M. Dawood (2013). A model for singlestation standard deviation using data from various tectonic regions, *Bull. Seism. Soc. Am.* **103**, 3149-3163, doi:10.1785/0120130030.

Ross, Z. E., Ben-Zion, Y., White, M. C., and F.L. Vernon (2016). Analysis of earthquake body wave spectra for potency and magnitude values: Implications for magnitude scaling relations. *Geophys. J. Int.*, **207**, 2, 1158-1164.

Sahakian, V. J., Baltay, A., Hanks, T. C., Buehler, J., Vernon, F. L., Kilb, D., and N. A. Abrahamson (2019). Ground motion residuals, path effects, and crustal properties: A pilot study in southern California. *J. Geophys. Res.*, **124**, 5738-5753.

Savage, M. K., and J. G. Anderson (1995). A local-magnitude scale for the western great basin-eastern Sierra Nevada from synthetic Wood-Anderson seismograms, *Bull. Seism. Soc. Am.* **85**, 1236-1243.

Shearer, P. M., Abercrombie R. E., Trugman D. T., and W. Wang (2019). Comparing EGF methods for estimating corner frequency and stress drop from p wave spectra, *J. Geophys. Res.* **124**, 3966-3986, doi:10.1029/2018jb016957

Somerville, P., and J. Yoshimura (1990). The influence of critical Moho reflections on strong ground motions recorded in San Francisco and Oakland during the 1989 Loma Prieta earthquake, *Geophys. Res. Lett.* **17**, 1203-1206

Spallarossa, D., D. Bindi, P. Augliera, & Cattaneo, M., 2002. An M_L scale in northwestern Italy, *Bull. Seism. Soc. Am.* **92**, 2205-2216.

Spallarossa, D., S. R. Kotha, M. Picozzi, S. Barani, and D. Bindi (2019). On-site earthquake early warning: A partially non-ergodic perspective from the site effects point of view, *Geophys. J. Int.* **216**, no. 2, 919-934, doi: 10.1093/gji/ggy470.

Thingbaijam, K.K.S., P.M. Mai, and K. Goda (2017). New empirical earthquake source-scaling laws, *Bull. Seism. Soc. Am.* **107**, 2225-2246

Trugman, D. T., and P. M. Shearer (2017), Application of an improved spectral decomposition method to examine earthquake source scaling in Southern California, *J. Geophys. Res. Solid Earth* **122**, 2890-2910, doi:10.1002/2017JB013971.

Trugman, D. T. (2020). Stress-Drop and Source Scaling of the 2019 Ridgecrest, California, Earthquake Sequence, *Bull. Seism. Soc. Am.* **XX**, 1-13, doi: 10.1785/0120200009

Uhrhammer, R. A., and E. R. Collins (1990). Synthesis of Wood-Anderson seismograms from broadband digital records, *Bull. Seism. Soc. Am.* **80**, 702-716.

Uhrhammer, R. A., M. Hellweg, K. Hutton, P. Lombard, A. W. Walters, E. Hauksson and D. Oppenheimer (2011). California Integrated Seismic Network (CISN) local magnitude determination in California and vicinity, *Bull. Seism. Soc. Am.* **101**, 2685-2693.

Villani M., and N. A. Abrahamson (2015). Repeatable site and path effects on the ground-motion sigma based on empirical data from southern California and simulated waveforms from the CyberShake platform. *Bull. Seism. Soc. Am.* **105**,2681-2695.

Wessel, P., W. H. F. Smith, R. Scharroo, J. F. Luis, and F. Wobbe (2013). Generic mapping tools: Improved version released, *Eos Trans. AGU* **94**, 409-410.

Wickham, H., (2016). ggplot2: Elegant Graphics for Data Analysis. Springer-Verlag New York, isbn:978-3-319-24277-4

Wickham, H., R. François, L. Henry, & Müller, K., (2018). dplyr: A Grammar of Data Manipulation. R package version 0.7.6. https://CRAN.R-project.org/package=dplyr

Zaccarelli, R., D. Bindi, A. Strollo, J. Quinteros and F. Cotton (2019). Stream2segment: an open source tool for downloading, processing and visualizing massive event-based seismic waveform datasets, *Seismol. Res. Lett.* **90**, 2028-2018, doi: 10.1785/0220180314

Zhang, Y., X. Zheng, Q. Chen, X. Liu, X. Huang, Y. Yang, Q. Xu, and J. Zhao (2020). Automatic Inversion of Rupture Processes of the Foreshock and Mainshock and Correlation of the Seismicity during the 2019 Ridgecrest Earthquake Sequence, *Seismol. Res. Lett.* **91**, 1556-1566.

Figures

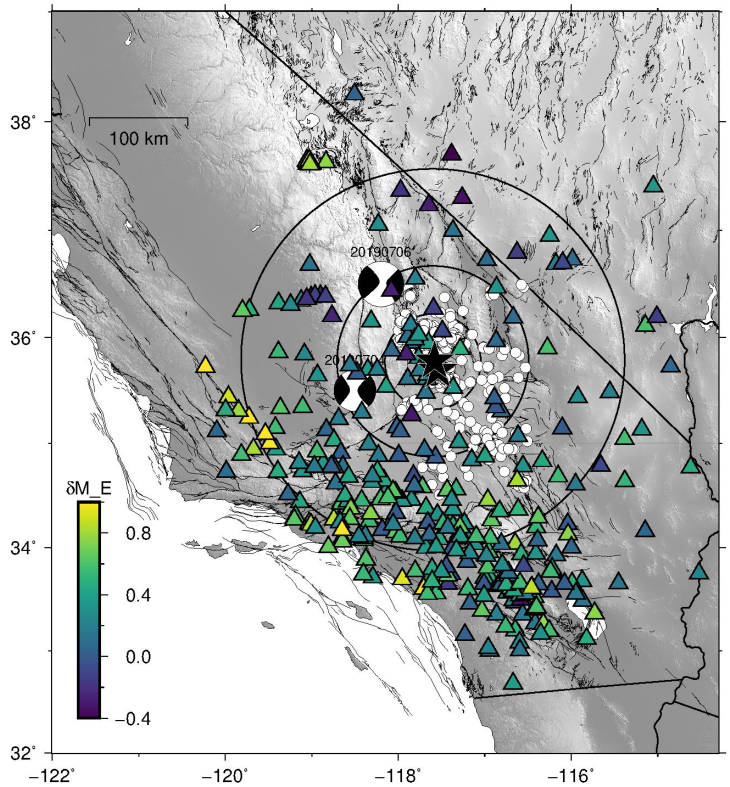

Figure 1: Map with earthquake (white circles) and station (triangles) locations. The legend reports the local magnitude station corrections δM_E for the east-west horizontal component. The focal mechanisms of the 2019, Mw 6.4 and 7.1 earthquakes are taken from GCMT (see Data and Resources). Three black circles are centered at the Mw 7.1 epicenter and have radius equal to 50, 100 and 200 km. The color version of this figure is available only in the electronic edition.

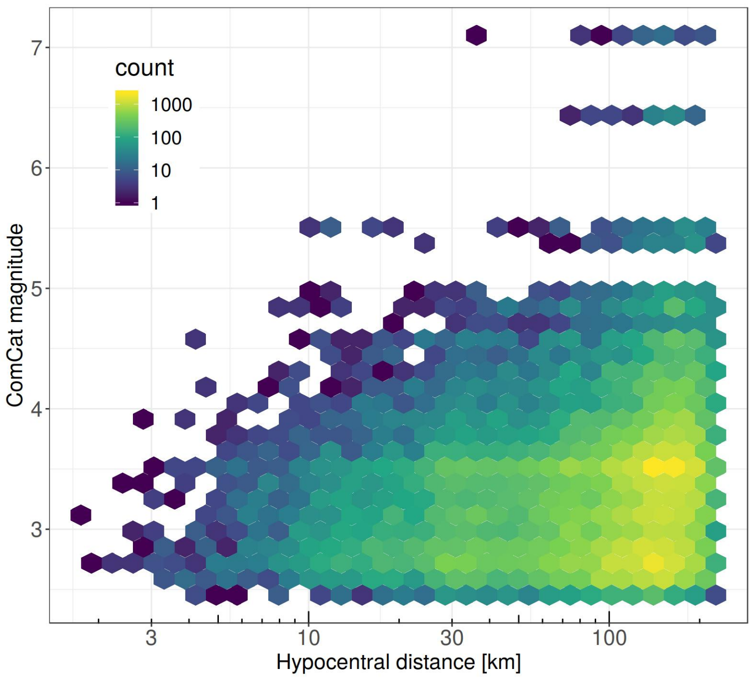

Figure 2: Catalog magnitude (ComCat) versus hypocentral distance density plot, where the legend reports the number of recordings (count) per magnitude-distance combination. The color version of this figure is available only in the electronic edition.

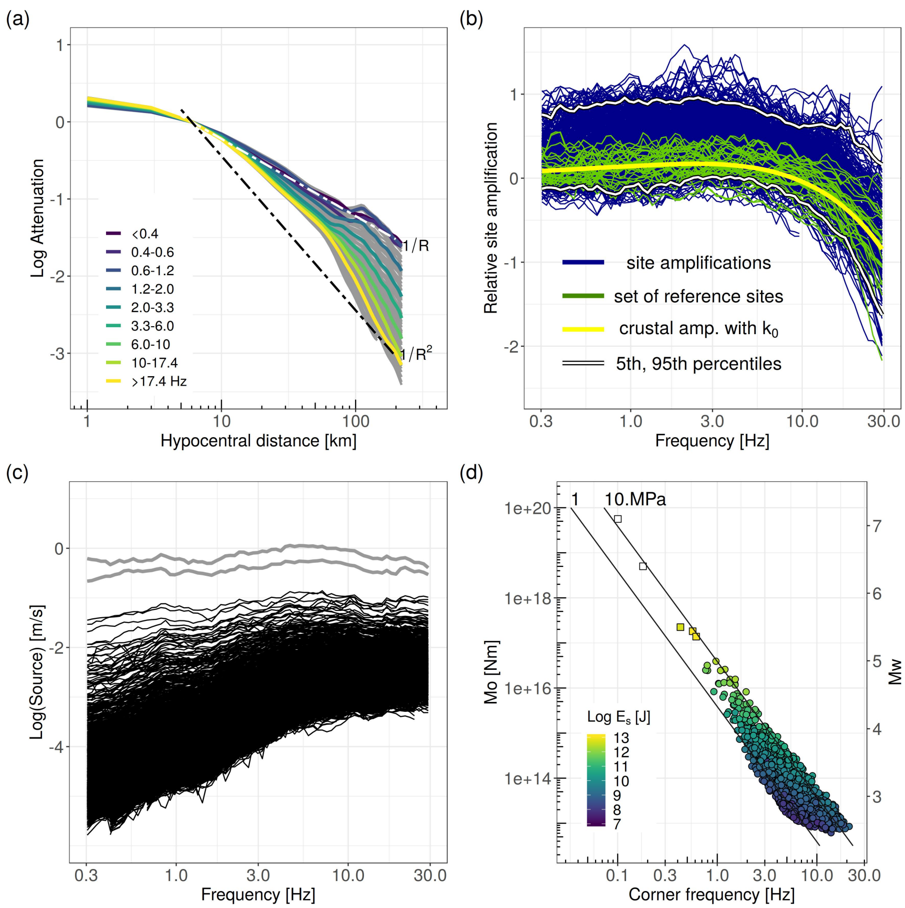

Figure 3: GIT results and source scaling. a) spectral attenuation curves for individual frequencies and average attenuation over different frequency ranges as indicated in the legend; the attenuation models corresponding to the inverse of the distance and its square (dashed lines) are provided for reference. b) site amplifications for all considered stations and for the set of reference stations; the reference model $\Gamma(f)$ of equation 3 corresponds to the crustal amplification for the B/C boundary and $k_0 = 0.034\ s$ Campbell and Boore (2016); for each frequency, the $5th$ and $95th$ percentiles of the spectral amplifications are evaluated considering all stations. c) Non parametric acceleration source spectra. d) Seismic moment versus corner frequency scaling for the best fit ω^{-2} models, where Es is the radiated energy estimated from the source spectra (not applied to the Mw 6.4 and 7.1 mainshocks). Squares indicate earthquakes with seismic moment fixed from ComCat. The color version of this figure is available only in the electronic edition.

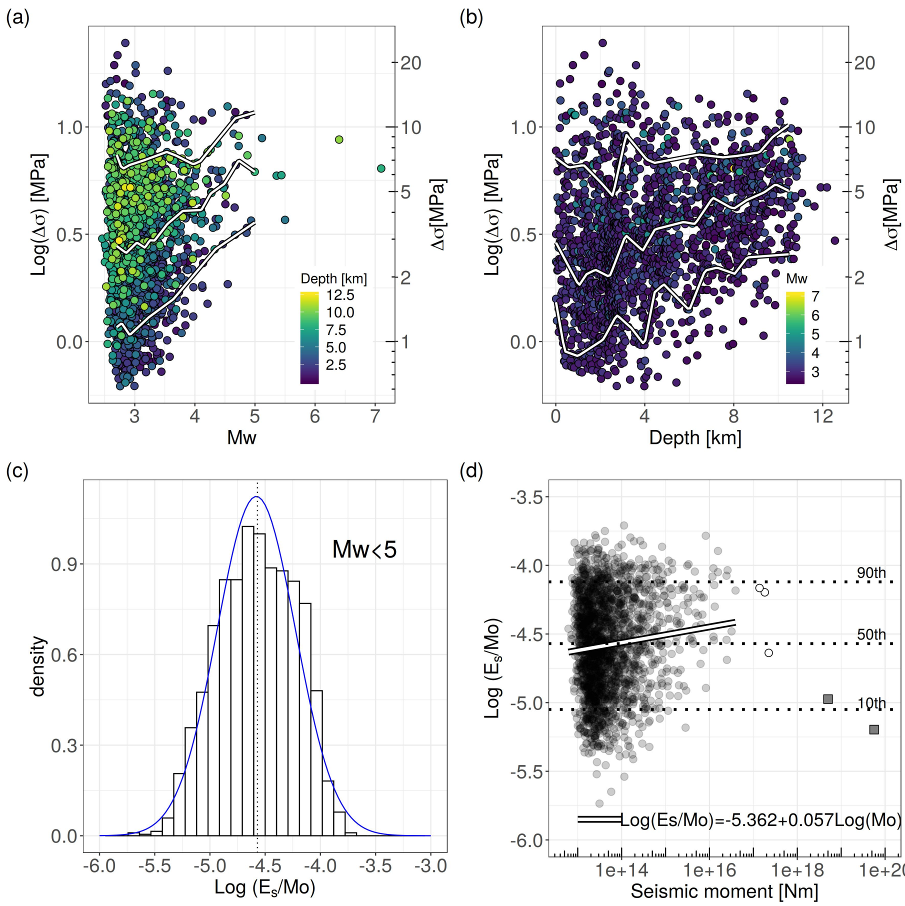

Figure 4: Source scaling. a) Stress drop versus moment magnitude, with depth values used to fill the symbols. b) Stress drop versus hypocentral depth, with Mw values used to fill the symbols. In panels a) and b), lines represent the result of quantile smoothing splines analysis Koenker et al. (1994), where the 10th, 50th and 90th percentiles are shown. c) Distribution of the logarithm of the radiated energy to seismic moment ratio (scaled energy) for earthquakes with Mw smaller than 5. d) Scaled energy versus seismic moment distribution with the best fit line indicating the scaling for $Mw < 5$; open circles indicate earthquakes with seismic moment constrained using Mw extracted from ComCat; the results for the Mw 6.4 and 7.1 mainshocks are indicated with rectangles (for these events, the energy have been estimated from teleseismic analysis). The color version of this figure is available only in the electronic edition.

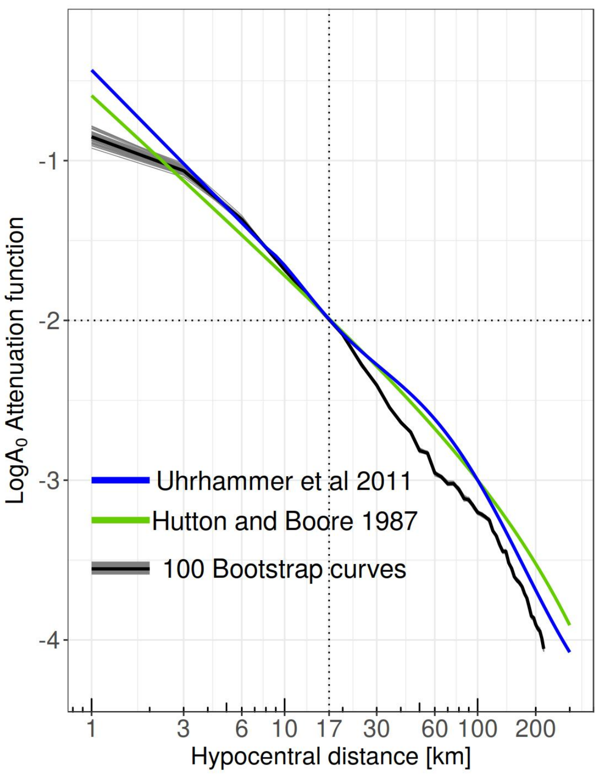

Figure 5: Non-parametric magnitude attenuation function $LogA_0$ calibrated in this study (bootstrap analysis) and models derived by Hutton and Boore (1987) and Uhrhammer et al. (2011). The color version of this figure is available only in the electronic edition.

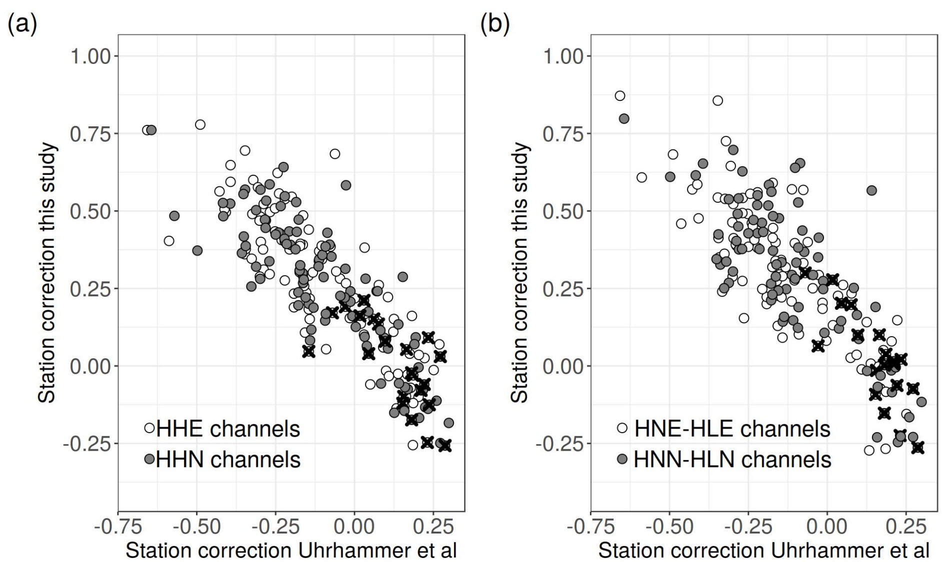

Figure 6: Station corrections obtained in this study versus those of Uhrhammer et al. (2011). In the left panel, the station correction for channels HH are compared (white for EW component, gray for NS component), in the right panel accelerometric stations are considered (using for Uhrhammer et al the station correction of the corresponding HH channel). Crosses are indicating the selected reference stations.

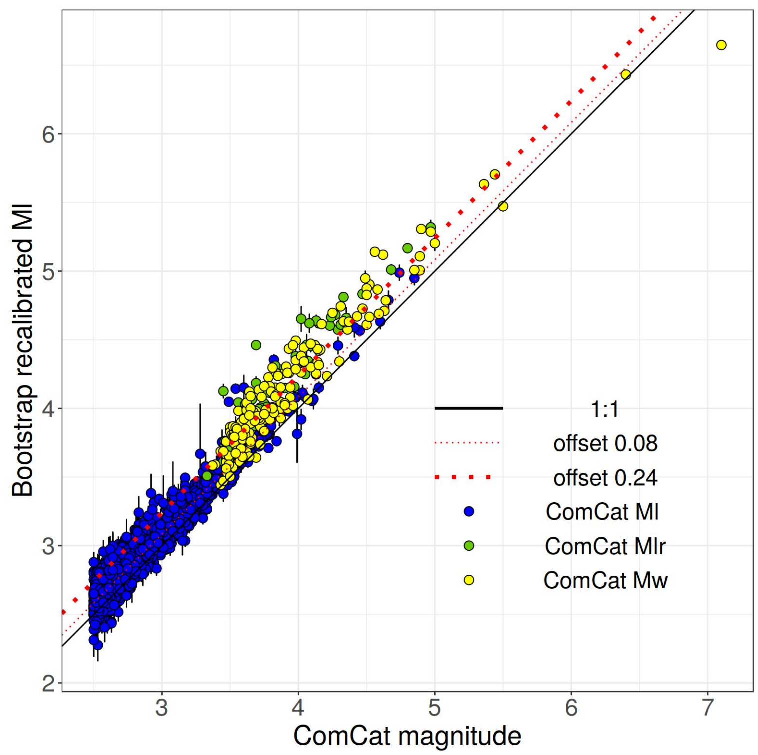

Figure 7: Comparison between the local magnitude calibrated in this study (from bootstrap analysis) and the catalog ones, which includes Ml, Mw, and Mlr magnitudes. The average offsets are shown as dashed and dotted lines (see legend). The color version of this figure is available only in the electronic edition.

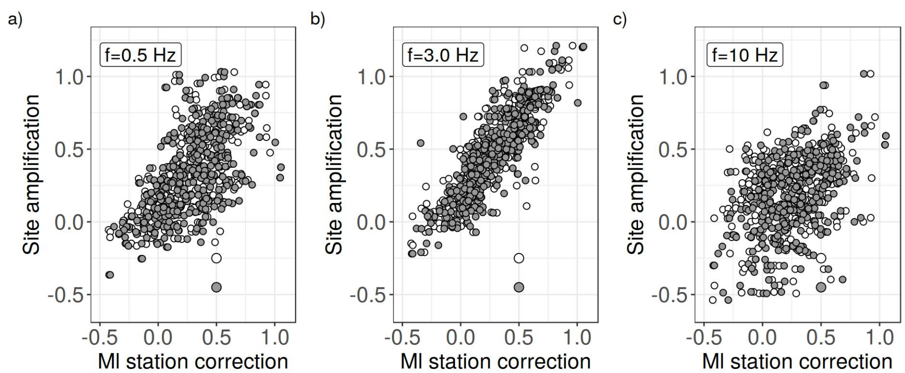

Figure 8: Site amplifications from GIT and local magnitude station corrections for three frequencies (0.5, 3.0, and 10 Hz), and the two hozitontal components (gray: East-West; white: North-South).

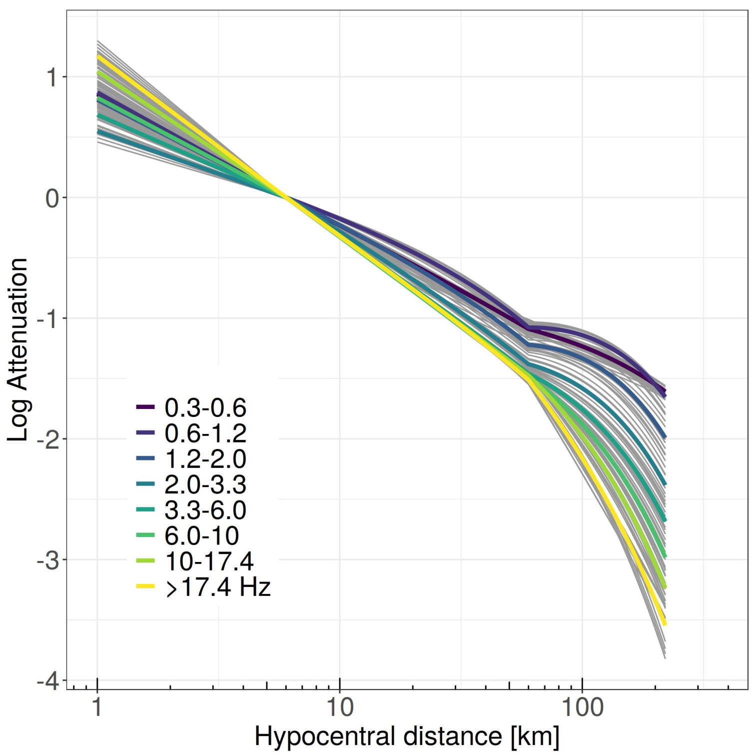

Figure 9: Distance scaling of the GMM. Thick curves are the average attenuation over frequency ranges as indicated in the legend. The color version of this figure is available only in the electronic edition.

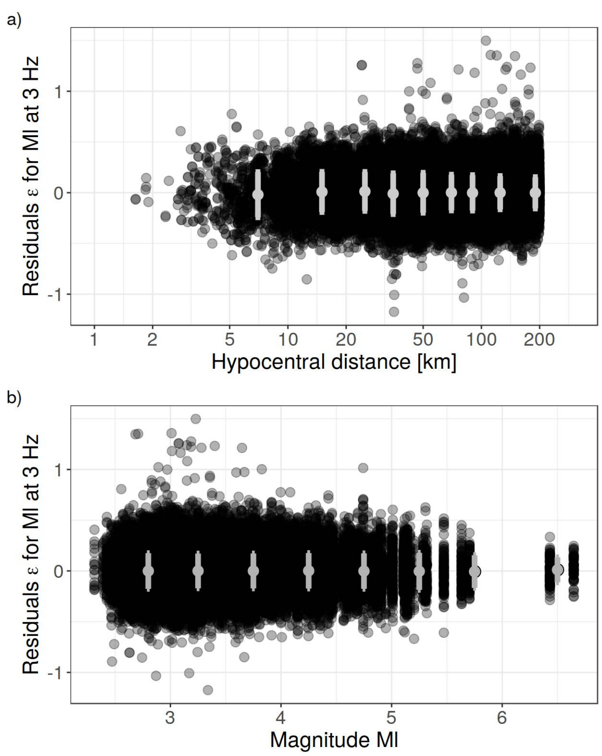

Figure 10: Distance and magnitude dependencies of the event station corrected residuals ϵ at 3Hz, considering the GMM derived using the local magnitude.

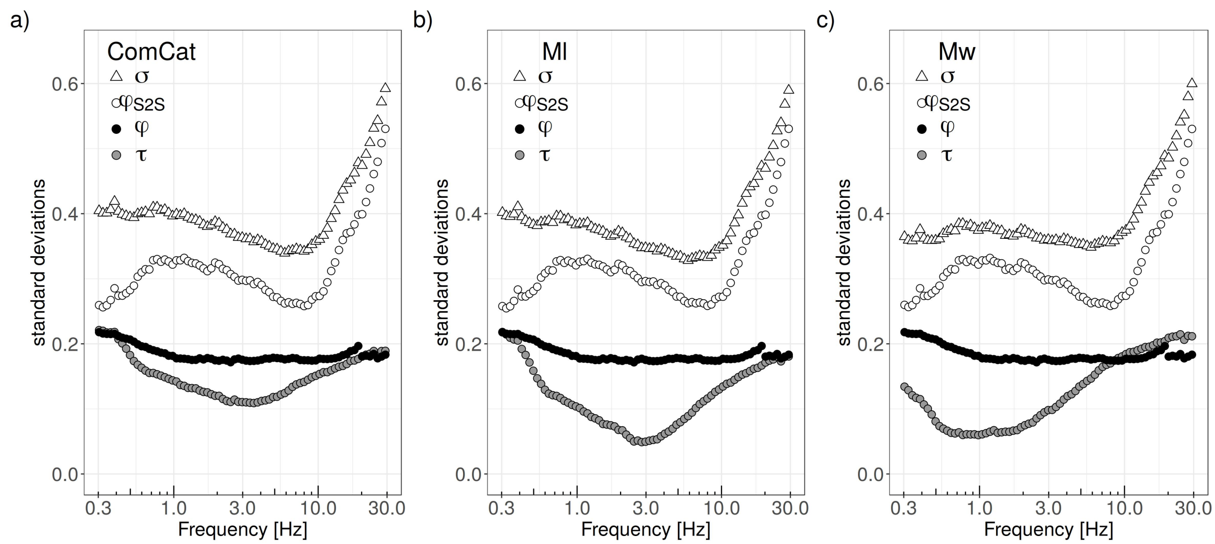

Figure 11: Standard deviations of GMMs calibrated considering the three different magnitude scales (ComCat, Ml and Mw, from left to right). The standard deviation of the inter-event residuals is indicated with τ.

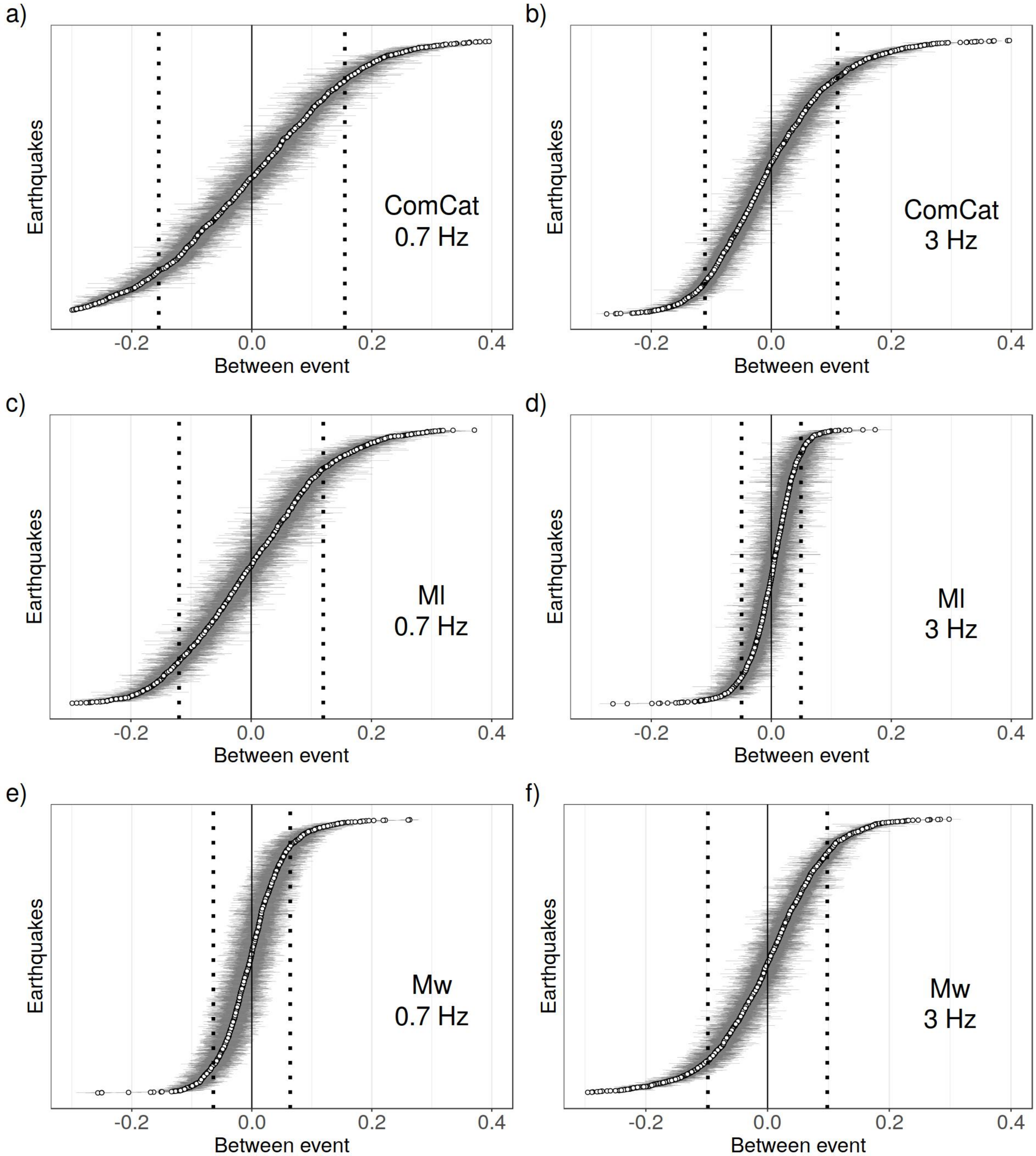

Figure 12: Inter-event residuals δBe for two frequencies (left: 0.7Hz; right: 3 Hz) and for the three magnitude scales considered in this study (ComCat, Ml and Mw from top to bottom). Dotted lines correspond to $\pm$ one τ standard deviation.

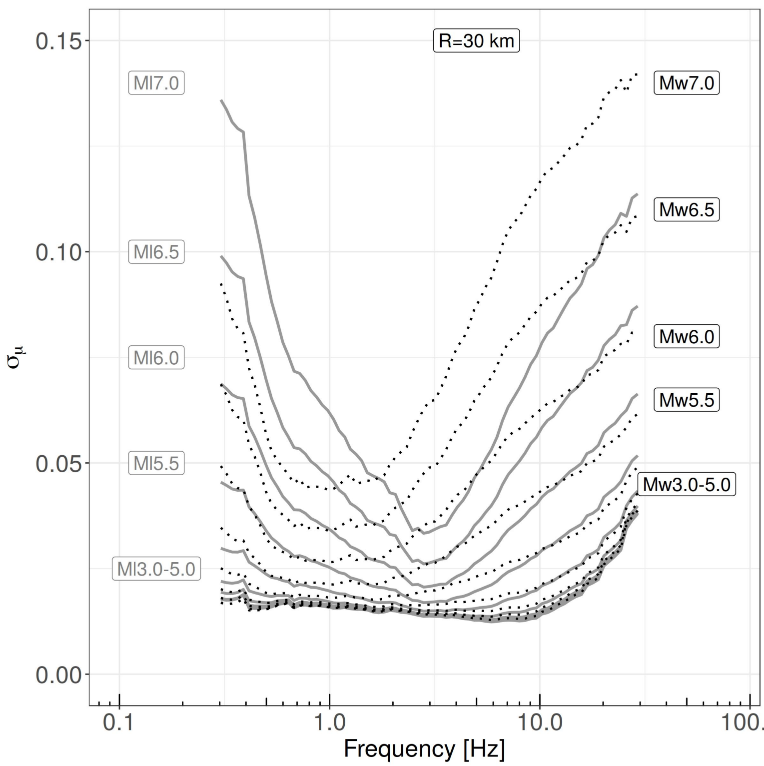

Figure 13: Standard deviations σ_μ considering Mw (black dotted) and Ml (gray), for scenarios corresponding to magnitudes between 3 and 7 and an hypocentral distance of 30 km.

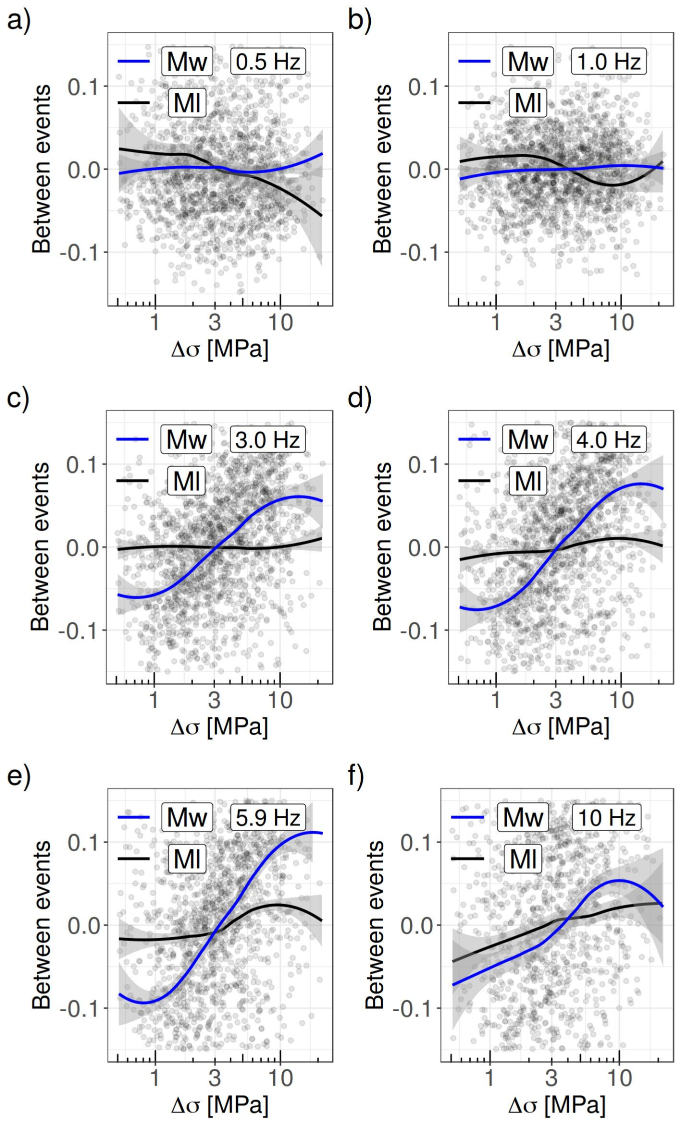

Figure 14: Inter events δBe trends with stress drop $\Delta\sigma$ for 6 frequencies between 0.5 and 10 Hz. The results for Ml and Mw are shown as indicated in the legend. The color version of this figure is available only in the electronic edition.

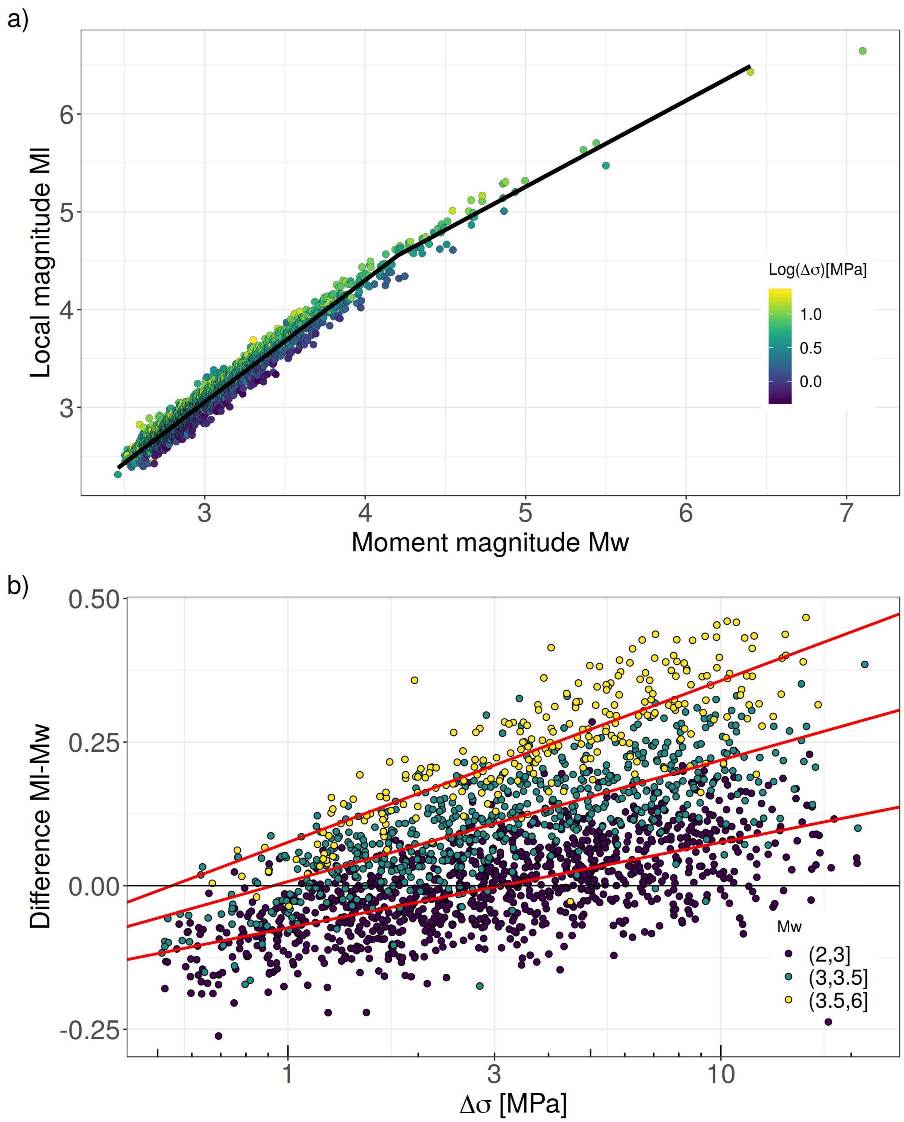

Figure 15: Comparison between Ml and Mw derived in this study. Top: result of the segmented regression; bottom: results of the linear fits between the magnitude differences and the logarithm of $\Delta\sigma$, considering three different magnitude ranges as indicated in legend. The color version of this figure is available only in the electronic edition.

Local and moment magnitude analysis in the Ridgecrest region, California: impact on inter-event ground motion variability

Dino Bindi , Riccardo Zaccarelli, Sreeram Reddy Kotha

Supplementary materials

The Supplementary materials document includes 7 Figures and 13 electronic tables.

Figure S1: Data distribution

Figure S1 shows the number of available recordings as function of the hypocentral distance, considering 4 different magnitude ranges as indicated within each frame. The density of stations in the Los Angeles basin increases the density of data points for distances above 100 km; the median distances, reported as vertical dotted lines, increase with magnitude (i.e., 104, 116, 136, and 147 km considering the magnitude ranges from the smallest to the largest, respectively) .

Figure S2: Reference site selection

In order to select the reference stations for the spectral decomposition (equation 3), we run a preliminary inversion setting the average amplification of all station to 1 (*i.e.*, $\Gamma(f) = 0$ in equation 3). Figure S2 shows the 5-95 percentiles of the amplifications obtained at all stations (blue). Those stations with 50th percentile of the cumulative amplification distribution lower than 0.8, a difference between the 95th and 5th percentiles lower than 1 and the 95th percentile lower than 1.5 are selected as candidate reference sites (red). Among all candidates, only those stations installed at sites with $vs_{30} \geq 700m/s$ are part of the final selection.

Figure S3: Comparison with ComCat magnitude

Figure S3 shows the comparison between the local and moment magnitudes derived in this study with those extracted from ComCat. The comparison between the moment magnitudes is shown in Figure S3a. We recall that the seismic moments derived in this study are constrained to agree on average with those from Comcat (equation 4 of the article). Figure S3b shows the comparison between the local magnitudes. The best fit model is shown as dotted line and the best fit linear model is indicated within the panel. In Figure S3c, the local versus moment magnitude relationship derived in this study is extrapolated towards magnitudes smaller than 2.5 (gray line) and compared to the model obtained by Trugman (2020) for Ridgecrest (dashed line); the gray ribbon corresponds to the Trugman (2020) model modified by applying the conversion between the ComCat local magnitudes and this study (i.e., the equation in Figure S3b) and adding an offet to Mw ranging between 0 and 0.2 magnitude units.

Figure S4: SmS arrivals

Figure S3 shows the efficency (i.e., the product of all conversion/reflection coefficients along the path) versus distance (left) and the arrival times of direct S and SmS waves considering CRUST2.0 model, the actual earthquake locations and distances. The top panels show the computations for events deeper than 10 km; results for depths between 5 and 10 km are shown in the bottom panels. Computations are performed using the module Cake of the Pyrocko library (Heimann et al. 2017) (see Data and Resources).

Figure S5: $\Delta\sigma$ distribution

Figure S4 shows the histogram of the $\Delta\sigma$ distribution (panel a) and the quantile-to-quantile plot (panel b) considering a normal distribution as theoretical model. In panel a, the median and standard deviation of the best fitting normal distribution are 0.48 and 0.30 for the logarithm in base 10 of $\Delta\sigma$ (indicated by vertical dotted lines), which correspond to a median value of $\Delta\sigma$ equal to 3 MPa with a factor 2 spread. Both the left and right tails of the empirical distribution are lighter than those of the normal distribution.

Figure S6: $\Delta\sigma$ dependencies on magnitude and depth

Figure S5 shows the dependency of $\Delta\sigma$ on magnitude and depth. The best fitting regression lines are obtained by performing a weighted least squares fit considering as weights either the inverse of the $\Delta\sigma$ variances (blue line) or the inverse of the number of records (red line) within magnitude (Figure S5a) or depth (Figure S5b) bins.

- The selected magnitude discretization is:
(2.6,2.9];(2.9,3.2];(3.2,3.5];(3.5,3.8];(3.8,4.1];(4.1,4.4];(4.4,5];(5,7.1]

- For each magnitude bin, the number of records (N) and the standard deviation (σ) of the stress drop are:

(N, σ)=(778,0.29);(575,0.29);(270,0.29);(131,0.28);(58,0.22);(30,0.22);(24,0.22);(6,0.14)

- The selected depth discretization is:

(0,1.5];(1.5,3];(3,4.5];(4.5,6];(6,7.5];(7.5,9];(9,10.5];(10.5,15] km

- For each depth bin, the number of records (N) and the standard deviation (σ) of the stress drop are:

(N, σ)=(285,0.32);(573,0.29);(287;0.30);(215,0.26);(197,0.23);(190,0.22);(137,0.21);(39,0.21)

The output of the regressions performed in R using the inverse of the number of points as weights are:

- rlm(formula = L10drop $\sim$ mw, data = subset(df, (mw $<=$ 5 & mw $>=$ 2.6)), weights = 1/Nmw)

(Value, Std. Error, t value)
Intercept: (0.0048,0.0323,0.1478)
Slope: (0.1544,0.0087,17.7179)
Residual standard error: 0.01419 on 1864 degrees of freedom

- rlm(formula = L10drop $\sim$ depth, data = subset(df, (mw $<=$7.1 & mw $>=$ 2.6)), weights = 1/Ndepth)

(Value, Std. Error, t value)
Intercept: (0.3294, 0.0118, 27.8387)
Slope: (0.0357, 0.0017, 20.6340)
Residual standard error: 0.01586 on 1921 degrees of freedom

Figure S7: Energy magnitude at teleseismic distances

We computed the energy magnitude Me of the two mainshocks following the procedure of (Di Giacomo et al. 2010) based on numerical Green's functions for the global 1D reference earth model AK135Q (Kennet et al. 1995; Montagner andKennett 1996). Figure S6 shows the distribution of the stations considered for the computation (left) and the obtained station magnitude values (right). The number of stations used for the Mw 6.4 and 7.1 events are 817 and 1209, respectively. The obtained Me values are (6.2 ± 0.2) and (6.8 ± 0.2).

Table S1: spectral attenuation curves

Table S1 (file table_S1.csv) lists the logarithm in base 10 of the non-parametric attenuation with distance curves. Distances in km are provided in the first column (dist[km]); each other column lists the attenuation at a given frequency indicated in the column name.

Table S2: source parameters

Table S2 (file table_S2.csv) lists the source parameters as follow: column 1 ComCat event ID; column 2 year_month_day of the origin time; column 3 hour:minute:seconds of the origin time; column 4 latitude of hypocentral location; column 5 longitude of hypocentral location; column 6 hypocentral depth in km; column 7 magnitude in ComCat; column 8 type of magnitude in ComCat; column 9 local magnitude calibrated in this study; column 10 logarithm in base 10 of seismic moment measure in Nm; column 11 corner frequency; column 12 kappa source in s; column 13 frequency from which kappa source is applied; column 14 moment magnitude derived in this study; column 15 radiated energy in J; column 16 stress drop in MPa.

Table S3: non-parametric $Log(A_0)$ attenuation

Table S3 (file table_S3.csv) lists the non-parametric local magnitude attenuation function $Log(A_0)$. Distances are listed in the first column, $Log(A_0)$ in the second column and the errors on $Log(A_0)$ evaluated through bootstrap analysis are given in the third column.

Table S4: magnitude station corrections

Table S4 (file table_S4.csv) lists the local magnitude station corrections.

Tables S5, S6, S7: GMM coefficients

Tables S5, S6, S7 (files table_S5.csv, table_S6.csv, table_S7.csv) list coefficients of the GMM developed for Mw, Ml and ComCat magnitude, respectively (equation 9 of the main article).

Tables S8, S9, S10: errors over the GMM coefficients

Tables S8, S9, S10 (files table_S8.csv, table_S9.csv, table_S10.csv) list the errors over the coefficients of the GMM developed for Mw, Ml and ComCat magnitude, respectively (equation 9 of the main article).

Tables S11, S12, S13: error for the GMM coefficients

Tables S11, S12, S13 (files table_S11.csv, table_S12.csv, table_S13.csv) list the standard deviations of the GMM developed for Mw, Ml and ComCat magnitude, respectively (equation 9 of the main article).

REFERENCES

Di Giacomo, D., S. Parolai,P. Bormann,H. Grosser,J. Saul, R. Wang and J. Zschau (2010). Suitability of rapid energy magnitude determinations for emergency response purposes, *Geophys. J Int.*, **180**, 361-374, doi: 10.1111/j.1365-246X.2009.04416.x

Heimann, S., M. Kriegerowski, M. Isken, S. Cesca, S. Daout, F. Grigoli, C. Juretzek, T. Megies, N. Nooshiri, A. Steinberg, H. Sudhaus, H. Vasyura-Bathke, T. Willey and T. Dahm (2017): Pyrocko - An open-source seismology toolbox and library. V. 0.3. GFZ Data Services. http://doi.org/10.5880/GFZ.2.1.2017.001

Kennett, B.L.N., E. R. Engdahl, and R. Buland (1995). Constraints on seismic velocities in the Earth from traveltimes,*Geophys. J Int.*, **122**, 108-124.

Montagner, J.-P. and B. L. N. Kennett (1996). How to reconcile body-wave and normal-mode reference Earth models? *Geophys. J Int.*, **125**, 229-248.

Trugman, D. T. (2020). Stress-Drop and Source Scaling of the 2019 Ridgecrest, California, Earthquake Sequence, *Bull. seism. Soc. Am.*, **XX**, 1-13, doi: 10.1785/0120200009

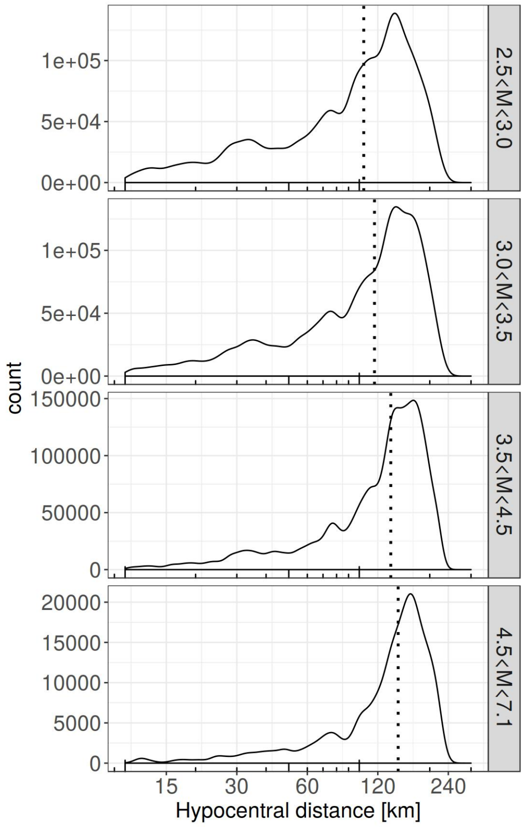

Figure S1. Distribution of recordings with hypocentral distance for the data set used to calibrate the local magnitude scale, splitting the data set into four different ComCat magnitude ranges; vertical dotted lines indicate the median distances.

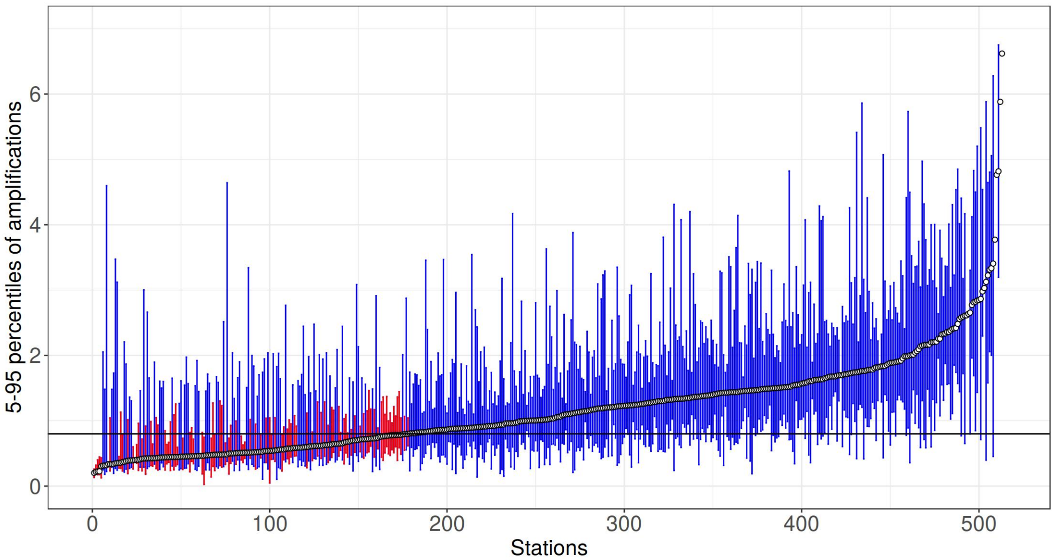

Figure S2. Selection of candidates as reference sites (red) for the spectral decomposition approach. The vertical blue bars indicate the 5th-95th interval of amplifications at the considered sites.

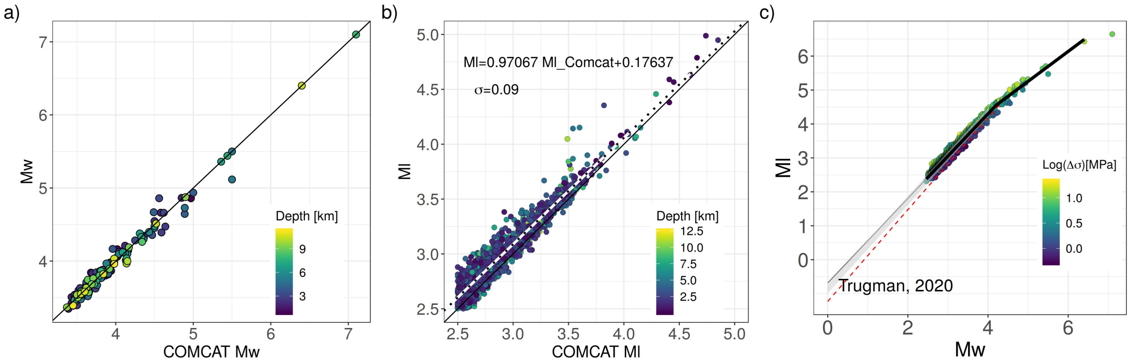

Figure S3. Comparison with ComCat magnitude. a) Moment magnitude derived in this study versus Mw in ComCat, with symbol filled according to hypocentral depth. b) Local magnitude derived in this study versus Ml in ComCat; the best fit line is shown as dotted line and the equation of the best fit linear model is given in the frame. c) The local versus moment magnitude relationship is extrapolated towards magnitudes smaller than 2.5 (gray line) and compared to the model derived by Trugman (2020) (dashed line); the gray ribbon corresponds to the Trugman (2020) model modified applying the conversion between ComCat and this study local magnitudes (equation in panel b) and adding an offet to Mw between 0 and 0.2 magnitude units.

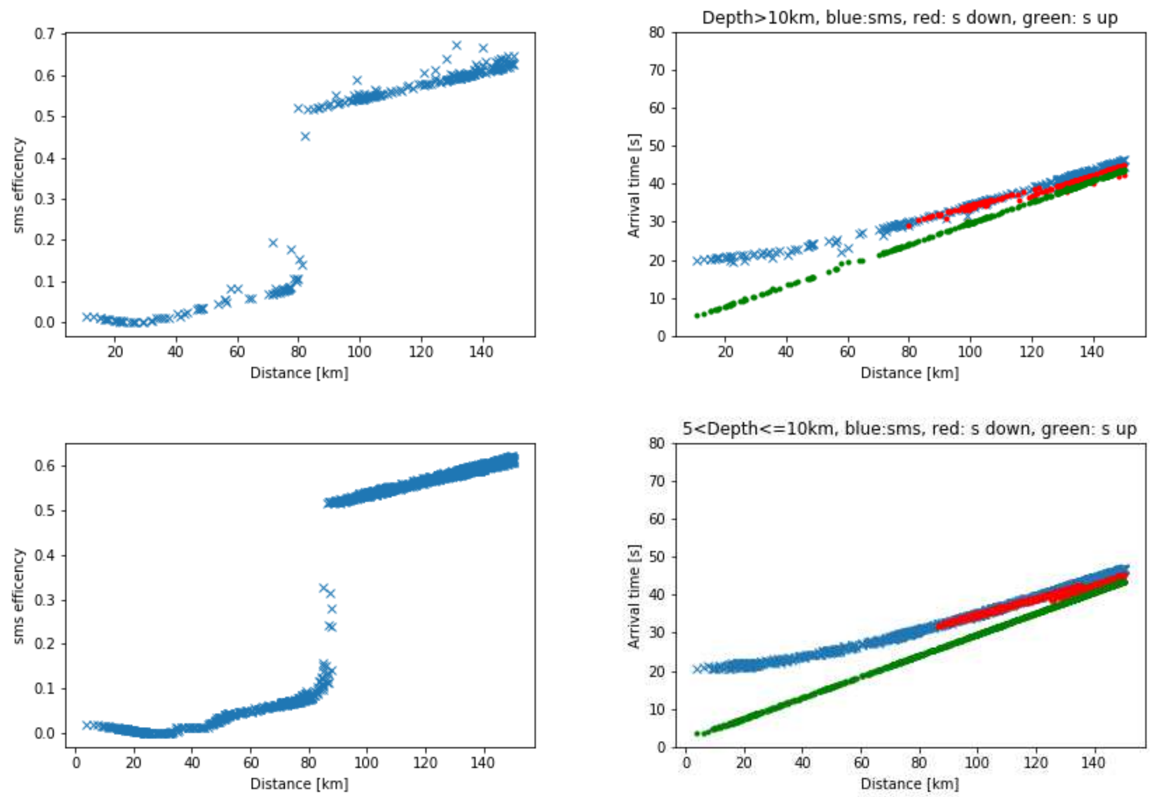

Figure S4. Analysis about efficiency (left) and travel times (right) of sms arrivals versus hypocentral distance, considering the CRUST2.0 velocity profile using Pyrocko software (Heimann et al. 2017). Top: depth > 10 km; bottom: $4 < depth \leq 10$ km. Crosses: SmS; circles: S waves leaving source either downward or upward. Computations are performed considering the actual earthquake locations and distances to the recording stations.

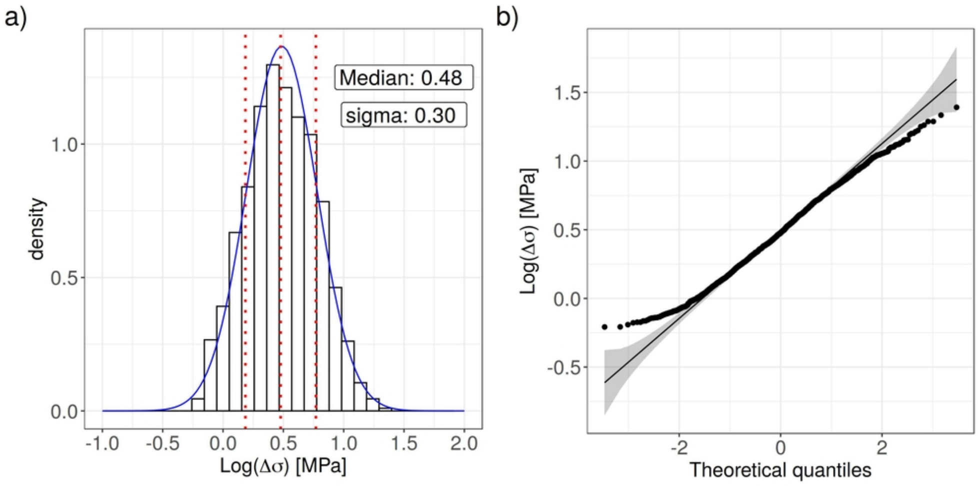

Figure S5 Distribution of $Log(\Delta\sigma)$ (panel a) and quantile-quantile plot (panel b) considering a normal distribution as reference model.

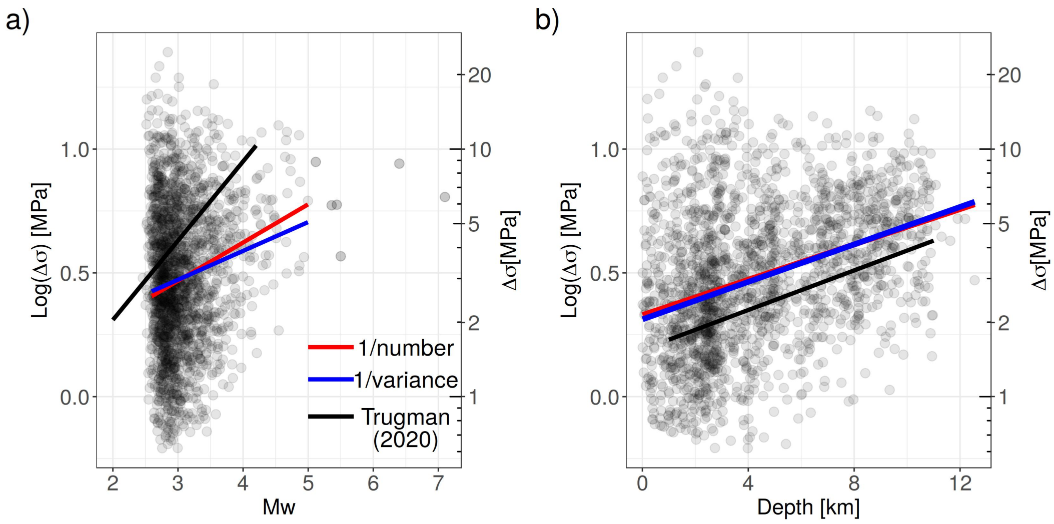

Figure S6. Stress drop scaling with moment magnitude (a) and depth (b). Straight lines represent the best fitting models using weighted least squares (red: weights proportional to the inverse of the number of recordings per magnitude or distance bins; blue: weights proportional to the inverse of $\Delta\sigma$ variance within each bin). Black lines represent the models derived by (Trugman 2020).

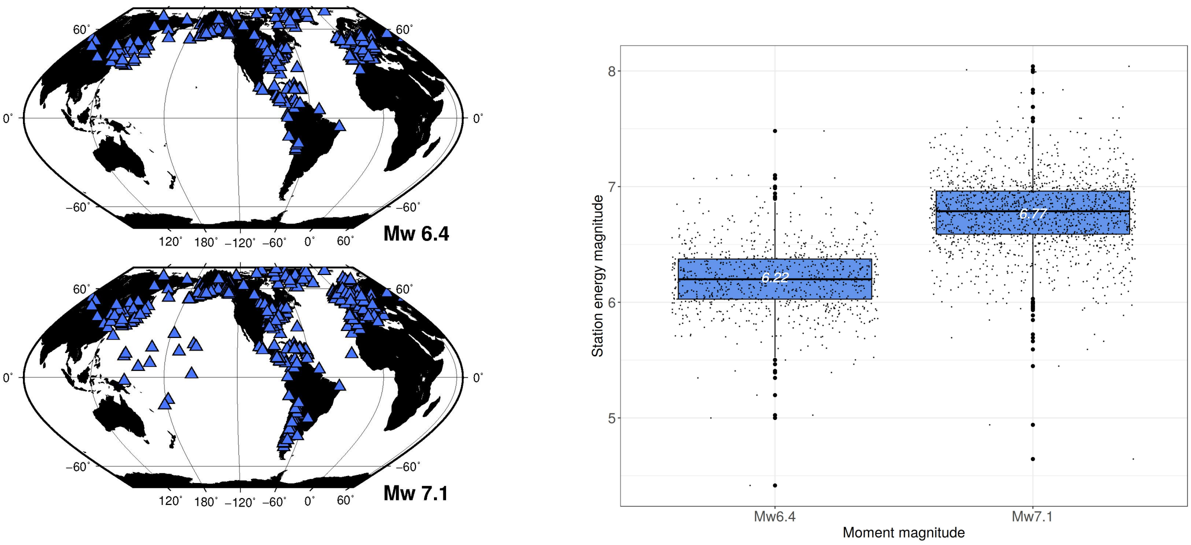

Figure S7. Energy magnitude computed at teleseismic distances for the Mw 6.4 and 7.1 mainshocks. Left: geographical distribution of the stations used for the assessment; right: distribution of the station magnitudes for the two events along with the box and whisker summary.